



저작자표시-비영리-변경금지 2.0 대한민국

이용자는 아래의 조건을 따르는 경우에 한하여 자유롭게

- 이 저작물을 복제, 배포, 전송, 전시, 공연 및 방송할 수 있습니다.

다음과 같은 조건을 따라야 합니다:



저작자표시. 귀하는 원저작자를 표시하여야 합니다.



비영리. 귀하는 이 저작물을 영리 목적으로 이용할 수 없습니다.



변경금지. 귀하는 이 저작물을 개작, 변형 또는 가공할 수 없습니다.

- 귀하는, 이 저작물의 재이용이나 배포의 경우, 이 저작물에 적용된 이용허락조건을 명확하게 나타내어야 합니다.
- 저작권자로부터 별도의 허가를 받으면 이러한 조건들은 적용되지 않습니다.

저작권법에 따른 이용자의 권리는 위의 내용에 의하여 영향을 받지 않습니다.

이것은 [이용허락규약\(Legal Code\)](#)을 이해하기 쉽게 요약한 것입니다.

[Disclaimer](#)

공학석사 학위논문

**Synthesis and characterization of metal-organic
framework MIL-100(Fe) for organic contaminants
removal from aqueous solutions**

수중 유기오염물질 제거를 위한 금속-유기
복합체 MIL-100(Fe)의 합성 및 제거 특성 연구

2021년 8월

서울대학교 대학원
생태조경·지역시스템공학부
지역시스템공학전공
장 호 영

**Synthesis and characterization of metal-organic
framework MIL-100(Fe) for organic contaminants
removal from aqueous solutions**

A THESIS
SUBMITTED TO THE DEPARTMENT OF LANDSCAPE
ARCHITECTURE AND RURAL SYSTEMS
ENGINEERING
AND THE COMMITTEE ON GRADUATE STUDIES OF
SEOUL NATIONAL UNIVERSITY IN PARTIAL
FULFILLMENT OF THE REQUIREMENTS FOR THE
DEGREE OF

MASTER OF ENGINEERING

By

HO YOUNG JANG

AUGUST, 2021

**Synthesis and characterization of metal-organic
framework MIL-100(Fe) for organic contaminants
removal from aqueous solutions**

수중 유기오염물질 제거를 위한 금속-유기
복합체 MIL-100(Fe)의 합성 및 제거 특성 연구

지도교수 김 성 배

이 논문을 공학석사 학위논문으로 제출함

2021년 6월

서울대학교 대학원

생태조경·지역시스템공학부 지역시스템공학전공

장 호 영

장 호 영의 공학석사 학위论문을 인준함

2021년 7월

위 원 장 _____

부위원장 _____

위 원 _____

I certify that I have read this thesis and that in my opinion it is fully adequate, in scope and quality, as thesis for the degree of Master of Engineering.

Chair of Commitee

I certify that I have read this thesis and that in my opinion it is fully adequate, in scope and quality, as thesis for the degree of Master of Engineering.

Vice-Chair of Commitee

I certify that I have read this thesis and that in my opinion it is fully adequate, in scope and quality, as thesis for the degree of Master of Engineering.

Member

Abstract

The aim of this study was to characterize the removal of contaminants from aqueous solution using a Metal-organic framework (MOF). The MOF is a porous crystalline complex made by a strong coordination bond between a metal cluster and an organic linker, which has large surface area, structural flexibility. MIL-100(Fe) was synthesized at room temperature with Iron (Fe) and Trimesic acid (H₃BTC). MIL-100(Fe) has environmental-friendly nature, high water stability, and great adsorption capacity.

In this study, the MIL-100(Fe) was applied as an adsorbent to removal of Rhodamine B (RhB) and Diclofenac (DCF) from aqueous solution. Batch experiments were conducted for RhB and DCF, respectively under single-parameter and multi-parameter experiment conditions. The maximum adsorption capacity for RhB is 61.845 mg g⁻¹ and DCF is 414. 581 mg g⁻¹. The main mechanisms are π - π interaction and electrostatic attraction for RhB removal, and π - π interaction and hydrogen bonding for DCF removal.

Further, Response surface methodology (RSM) and Artificial neural network (ANN) were employed to model and optimized the RhB and DCF removal in the range of the CCD matrix as multi-parameter models. In RSM modeling, the cubic regression model was developed for RhB removal and the regressor variable of pH had a larger coefficient value indicating that pH had a highest impact on the RhB removal rate. The optimum RhB removal rate was found at pH 5.3, adsorbent dose 2.0 g L^{-1} , initial RhB concentration 73 mg L^{-1} through the prediction of the modeled ANN with topology 3:8:1. The optimum DCF removal rate was found at initial pH 6.1, adsorbent dose 0.5 g L^{-1} , initial DCF concentration 63 mg L^{-1} , temperature 22°C through the prediction of the modeled ANN with topology 4:7:6:2.

Study results indicate that the MIL-100(Fe) synthesized at room temperature shows high adsorption capacity for RhB and DCF removal from synthetic water, and the RSM and ANN model could be successfully optimize and predict for RhB and DCF removal as multi-parameter models.

Keywords : Metal organic framework, MIL-100(Fe), Adsorption, Rhodamine B, Diclofenac, Response surface methodology, Artificial neural network

Student Number : 2019-22277

Contents

Abstract	i
Contents.....	iv
List of Tables	vii
List of Figures	x
1. Introduction	1
1.1. Background.....	1
1.1.1. Metal-organic framework (MOF)	3
1.1.2. Contaminants	6
1.1.3. Multi-parameter model.....	12
1.2. Objective.....	14
2. Literature Review.....	15
2.1. Adsorption of contaminants from aqueous solution using MOFs	15
2.2. Dye adsorption using MOFs	18
2.3. Pharmaceutical adsorption using MOFs	23

3. Materials and Methods 30

3.1. Synthesis of MIL-100(Fe) at room temperature	30
3.2. Characterization of MIL-100(Fe)	33
3.3. RhB adsorption from synthetic water	35
3.3.1. Single-parameter experiments for RhB removal	35
3.3.2. Multi-parameter experiments for RhB removal.....	39
3.4. DCF adsorption from synthetic water.....	43
3.4.1. Single-parameter experiments for DCF removal.....	43
3.4.2. Multi-parameter experiments for DCF removal	48
3.5. Data analysis for single-parameter experiments.....	51
3.6. Multi-parameter modeling through RSM and ANN	54
3.6.1. Response surface methodology (RSM)	54
3.6.2. Artificial neural network (ANN)	56

4. Results and Discussion 60

4.1. Characterization of MIL-100(Fe)	60
4.2. Adsorption studies for RhB	72
4.2.1. Single-parameter experiments for RhB removal	72
4.2.2. Multi-parameter modeling using RSM	80
4.2.3. Multi-parameter modeling using ANN.....	87
4.3. Adsorption studies for DCF	99
4.3.1. Single-parameter experiments for DCF removal.....	99
4.3.2. Multi-parameter modeling using ANN.....	109

5. Conclusions	121
6. References	124
국문 초록	140

List of Tables

Table 1. Studies for contaminants adsorption form aqueous solutions using MOFs	17
Table 2. Studies for dye adsorption form aqueous solutions using MOFs synthesized by hydrothermal method	21
Table 3. Studies for pharmaceutical adsorption form aqueous solutions using MOFs synthesized by hydrothermal method	26
Table 4. Batch experiment conditions for RhB removal	37
Table 5. CCD levels of input variables ($\alpha=2$) for RhB adsorption	41
Table 6. Designed matrix conditions for RhB adsorption	42
Table 7. Batch experiment conditions for DCF removal.....	45
Table 8. CCD levels of input variables ($\alpha=2$) for DCF adsorption	49
Table 9. Designed matrix conditions for DCF adsorption.....	50
Table 10. Reduced Fe ions mass percentage (%) after the reaction (24hr)	71
Table 11. Model parameters of Langmuir, Freundlich and Redlich- Peterson isotherm model obtained from model fitting for RhB isotherm data	76
Table 12. Model parameters of pseudo first, pseudo second, Elovich kinetic model obtained from model fitting for RhB kinetic data .	77
Table 13. Thermodynamic model parameters obtained from RhB adsorption experiments.....	78

Table 14. Observed removal rates and predicted values from RSM modeling for RhB adsorption	82
Table 15. ANOVA results of full cubic regression model from RSM ..	83
Table 16. Comparison of network topologies with various hidden layers and neurons for RhB removal.....	90
Table 17. Values of weights and biases for each layer and neuron in equation (17).....	92
Table 18. Observed removal rates and predicted values from ANN modeling for RhB adsorption (Topology 3:6:1).....	93
Table 19. Additional experimental conditions along with observed and predicted from the ANN model values for RhB removal rates	95
Table 20. Optimum condition for RhB removal by the MIL-100(Fe) from ANN model	98
Table 21. Model parameters of Langmuir, Freundlich and Redlich-Peterson isotherm model obtained from model fitting for DCF isotherm data	104
Table 22. Model parameters of pseudo first, pseudo second, Elovich kinetic model obtained from model fitting for DCF kinetic data	105
Table 23. Thermodynamic model parameters obtained from DCF adsorption experiments.....	106
Table 24. Comparison of network topologies with various hidden layers and neurons for DCF removal	113
Table 25. Values of weights and biases for each layer and neuron in	

equation (19).....	114
Table 26. Observed removal rates, final pH and predicted values from ANN modeling for DCF adsorption (Topology 4:7:6:2).....	115
Table 27. Additional experimental conditions along with observed and predicted from the ANN model values for DCF removal rates and final pH.....	117
Table 28. Optimum condition for DCF removal by the MIL-100(Fe) from ANN model	120

List of Figures

Fig. 1. Chemical structure of Rhodamine B (RhB): (a) at acidic pH; (b) at neutral pH(>4).....	8
Fig. 2. Chemical structure of Diclofenac sodium (DCF): (a) before dissolving in water; (b) undissociated soluble form and/or undissociated precipitated form.....	11
Fig. 3. A schematic diagram of the MIL-100(Fe) synthesis process at room temperature.....	32
Fig. 4. Calibration curve obtained with RhB standard solutions.....	38
Fig. 5. Species distribution of DCF in response to solution pH at a total DCF concentration of 80 mg L ⁻¹	46
Fig. 6. Calibration curve obtained with DCF standard solutions	47
Fig. 7. Schematic diagram of experimental design and modeling analysis with the tools	58
Fig. 8. Artificial neural network (ANN) architecture	59
Fig. 9. FESEM images of MIL-100(Fe) according to various pH: (a) at pH 2; (b) pH 4; (c) pH 6; (d) pH 8; (e) pH 10; (f) pH 12	63
Fig. 10. EDS spectra of the MIL-100(Fe)	64
Fig. 11. XRD pattern of the MIL-100(Fe) with various pH	65
Fig. 12. ELS spectra (zeta potential) of the MIL-100(Fe).....	66
Fig. 13. N ₂ adsorption-desorption isotherms of the MIL-100(Fe)	67
Fig. 14. TGA curve of the MIL-100(Fe)	68

Fig. 15. XPS spectra of the MIL-100(Fe): (a) wide scan; (b) high-resolution scan of C 1s	69
Fig. 16. FT-IR spectra of the MIL-100(Fe)	70
Fig. 17. Batch studies for RhB removal: (a) isotherm; (b) kinetic; (c) thermodynamic; (d) pH	75
Fig. 18. Schematic diagram for RhB and DCF removal mechanism by the MIL-100(Fe).....	79
Fig. 19. Diagnostic plot between observed and predicted removal rates from the RSM model	85
Fig. 20. Interaction effect of input variables on the RhB removal rate	86
Fig. 21. Schematic diagram of artificial neural network (ANN) structure: (a) for the RhB adsorption; and (b) DCF adsorption.....	91
Fig. 22. Linear fit for experimental and predicted RhB removal rate ..	94
Fig. 23. Diagnostic plot between observed and predicted values from additional experiments for RhB removal rate	96
Fig. 24. Relative importance of three input variables on the RhB removal rate	97
Fig. 25. Batch studies for DCF removal: (a) isotherm; (b) kinetic; (c) thermodynamic; (d) pH	103
Fig. 26. The wide scan XPS spectra of the MIL-100(Fe): (a) before and; (b) after adsorption	107
Fig. 27. The FTIR spectra of the MIL-100(Fe) before and after	

adsorption	108
Fig. 28. Linear fit for experimental and predicted DCF removal rate and final pH.....	116
Fig. 29. Diagnostic plots between observed and predicted values from additional experiments: (a) DCF removal rate; and (b) final pH	118
Fig. 30. Relative importance of four input variables on the DCF removal rate	119

1. Introduction

1.1. Background

Water environment is polluted by byproducts of various industries, including agriculture or by chemicals generated from people's lives. Various pollutants such as heavy metals, radioactive substances, organic dyes, and pharmaceuticals and personal care products exist in water. As an example, the continuous use of fertilizers has significantly contributed to increase the level of heavy metals and metalloids in soil and groundwater. Fertilizers contain phosphates for the growth of crops, and the level of phosphate is increasing due to excessive discharge from agricultural runoff into the water. The high level of phosphate concentration can cause eutrophication of water which ultimately leads to imbalance of aquatic ecology (Nehra et al., 2019). As another example, heavy metal contamination such as chromium (Cr), arsenate (As), antimony (Sb), and lead (Pb) of surface water or groundwater occurs by wastewater discharge from leather, paint, textile, dyeing industries. Heavy metal pollution has long been regarded as a serious issue of environmental pollution due to its easy accumulation, poor degradability,

and biologically related toxicity (Fang et al., 2018). Since other pollutants such as dyes or pharmaceuticals also adversely affect the aquatic environment and aquatic organisms in various ways, treatment of contaminants is essential.

Several processes including biological, physical and chemical are used for treating wastewater. Currently, methods used for contaminants removal from aqueous solutions include ion exchange, chemical precipitation, coagulation/flocculation, membrane filtration, photocatalytic degradation, adsorption and so on. Amongst them, adsorption method is more frequently applied because of low cost, easy application, environmental friendliness, and high efficiency (Fang et al., 2018; Zhang et al., 2019(1); Zhang et al., 2019(2)). Further, an effective adsorbent for contaminants removal should have high performance, rapid adsorption, cost effectiveness, good water stability, and environmental friendliness.

1.1.1. Metal-organic framework (MOF)

Granular or powdered activated carbon is commonly used in water and wastewater treatment as an adsorbent, relatively new adsorbents such as carbon nanotubes, graphene-based adsorbents, and metal-organic frameworks (MOFs) have been investigated recently for removal of various contaminants from aqueous solutions (Joseph et al., 2019). MOFs are three-dimensional crystalline complex made by a strong coordination bond between a metal (Fe, Zn, Zr, Cu, Al etc.) and an organic linker (Trimesic acid, Phthalic acid etc.) (Feng et al., 2018; Kokcam-Demir et al., 2020). MOF is a porous material, and have an easy tunability in their shape and pore size (\AA - nm) by employing various organic linkers and metal ions (Zhou et al., 2014). It has high adsorption capacity due to its large specific surface area, has structural flexibility, and has the advantage of easy modification like attachment of functional group (-OH group, -NH₂ etc.), magnetizing MOF (Fe₃O₄@MIL-100(Fe)), widening of the specific surface area through calcination etc. MOF is a material that can be used not only as an adsorbent, but also for various purposes such as gas storage, drug delivery, sensors, and catalysts (Furukawa et al., 2013; Tehrani et al., 2017). Among them,

focusing on the MOF as an adsorbent, MOF is capable of adsorbing various target substances such as heavy metals (As, Pb, Hg, Cd, Cr etc.), radioactive substances (U, Se, Cs etc.), nutrients like nitrate or phosphate ion, organic dyes (Methylene blue(MB), RhB etc.), and pharmaceuticals and personal care products (Ibuprofen, DCF etc.) (Cai et al., 2016; Seo et al., 2016; Wang et al., 2017; Zhan et al., 2018; Zhang et al., 2019; Esrafilı et al., 2019a, 2019b). The nomenclature of MOF is determined by the type of metals and organic linkers and structural topology, and is also named after the organization that synthesized the MOF. In this study, MIL (Materials of Institut Lavoisier)-100(Fe) was selected among the various MOFs and synthesized for removal of RhB and DCF from aqueous solutions. MIL-100(Fe) is a MOF made using Iron (Fe) and Trimesic acid (H_3BTC). MIL-100(Fe) has environmental-friendly nature, greater specific surface area, and higher water stability than other MOF-based adsorbents (Fang et al., 2018; Nehra et al., 2019; Zhang et al., 2019). The most conventional MIL-100(Fe) synthesis is conducted by hydrothermal synthesis method at temperatures as high as 150 – 180 °C. However, MIL-100(Fe) synthesized at room temperature has a simpler process, does not require an apparatus such as Teflon-lined steel

autoclave and heating mantle, and has a yield of about 2 – 3 times higher than hydrothermal synthesized MIL-100(Fe). Guesh et al. (2017), which synthesized MIL-100(Fe) at room temperature, conducted a study to remove Methyl orange using MOF as a photocatalyst.

1.1.2. Contaminants

Organic contaminants including dye, humic acid, phenolic compounds, surfactants, and pharmaceuticals are important pollutants in wastewaters. The presence of organic contaminants in water may produce toxic chemicals during disinfection. In this study, dye and pharmaceutical, which are widely used in industry and have the potential to adversely affect the health of aquatic organisms and human health due to their toxicity, were selected as target substances to be adsorbed among contaminants that pollute water.

The first contaminant is Rhodamine B (RhB), which is an organic dye that is widely used in industries such as textile industry, leather dyeing factory, rubber or paint making factory. In the case of RhB, it is widely used as a tracer because of its colorant or a fluorescent material. Organic dyes generated in industrial can cause water pollution by giving it color, and especially RhB have toxic and carcinogenic (Bagheri et al., 2013; Sharma et al., 2017), so it can significantly affect aquatic organisms and human health as well (Zhu et al., 2016; Fan et al., 2018). The process of treating the organic dye is essential because in general,

dyeing wastewater is a non-degradable wastewater that is not easily treated by a biological treatment process, and it must meet the standards for discharge of industrial wastewater. Among the treatment technologies, adsorption is widely applied for the removal of dyes in wastewater due to its simplicity and cost-effectiveness (Haque et al., 2011; Adeyemo et al., 2012; Zhu et al., 2016; Fan et al., 2018). The pK_a value of RhB is 3.7, molar weight is 479 g mol^{-1} , and chemical structure of RhB is presented in Fig. 1. As shown in Fig. 1a, it exhibits the properties of cationic dye at acidic pH because of its amino xanthene group (N^+), and it exhibits the properties of zwitterionic dye at $pH > 4$ due to deprotonated carboxyl group (COO^-) in Fig. 1b.

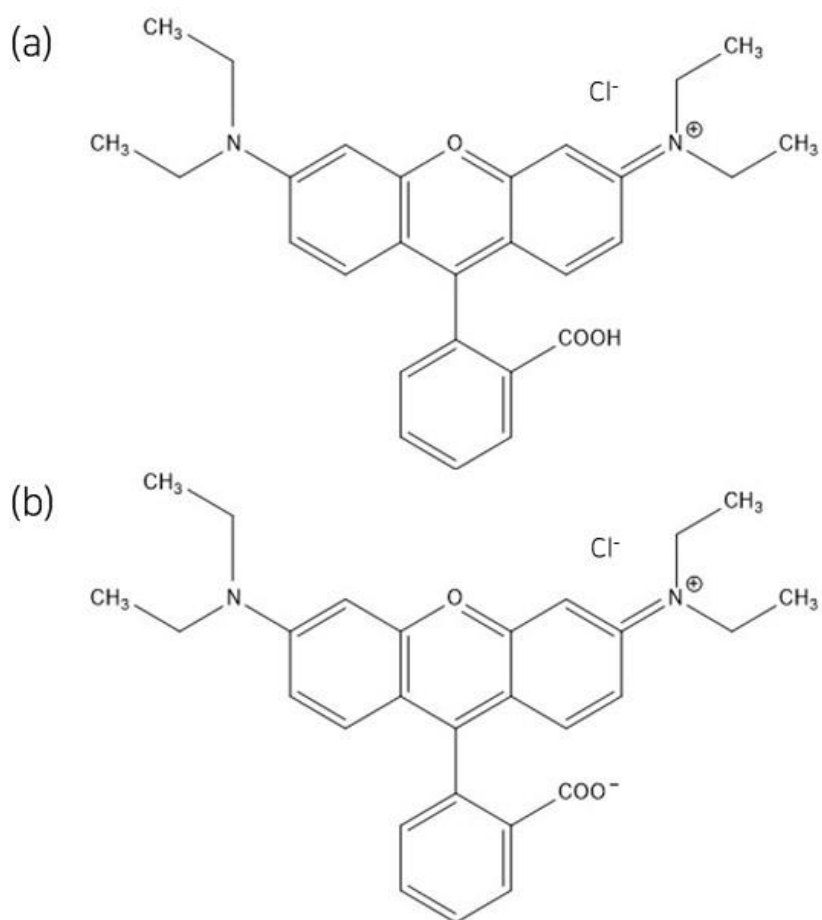


Fig. 1. Chemical structure of Rhodamine B (RhB): (a) at acidic pH;
(b) at neutral pH(>4)

The second contaminant is one of pharmaceutical, Diclofenac (DCF). DCF is one of the nonsteroidal anti-inflammatory drugs (NSAIDs) which is remedy prescribed worldwide and classified as over-the-counter drug. DCF is widely used to treat pain and inflammation such as gout and arthritis, and is used by oral administration or by administration to the skin (an idiomatic name is Voltaren) (Antunes et al., 2012; Ghemit et al., 2019). DCF has a high solubility in water and a pK_a value of 4.15, and molecular weight of 296 g mol^{-1} (Wu et al., 2020). The spillage of waste drugs into the environment became known for the first time in the 1970s when the Environment Protection Agency (EPA) of the United States published a report on the presence of waste drugs in the environment. It is detected from soil, rivers, groundwater or even drinking water and several drugs have been designated as potential water pollutants (Benotti et al., 2009). According to a drug consumption survey conducted by the Agency for Healthcare Research and Quality (AHRQ) in the U.S. in 2020, DCF was ranked among more than 8 million prescriptions annually for the last 5 years as of 2018. As the amount of consumption is shown, it can be confirmed that there is a steady demand for it. The annual output of DCF was 5989 kg by the National Institute of

Environmental Sciences' net domestic drug production survey (Oh et al., 2009). An average of 1276 ng L⁻¹ was also detected in the discharged water from the sewage treatment facility. If it exceeds 1000 ng L⁻¹, a risk assessment is required (Oh et al., 2009). Pharmaceutical cause potential adverse effects on human health and the ecosystem even at very low concentrations (Wang et al., 2019; Zhu et al., 2019; Wang et al., 2020). Several methods including ozonation, photo-fenton oxidation, biodegradation, photocatalyst, electrochemical degradation, and adsorption have been applied to remove DCF from water and wastewater (He et al., 2014; Wang et al., 2016; De et al., 2017; Wang et al., 2017; Wang et al., 2019; Wang et al., 2020(1); Wang et al., 2020(2); Zhuan et al., 2020; Liu et al., 2021). Adsorption is considered a promising method for removal of DCF from water because it is simple, cost-effective, and easy to operate (Binaeian et al., 2020). Chemical structure of DCF is presented in Fig. 2. Fig. 2a is the DCF form before dissolving in water and Fig. 2b is the undissociated soluble form and/or undissociated precipitated form.

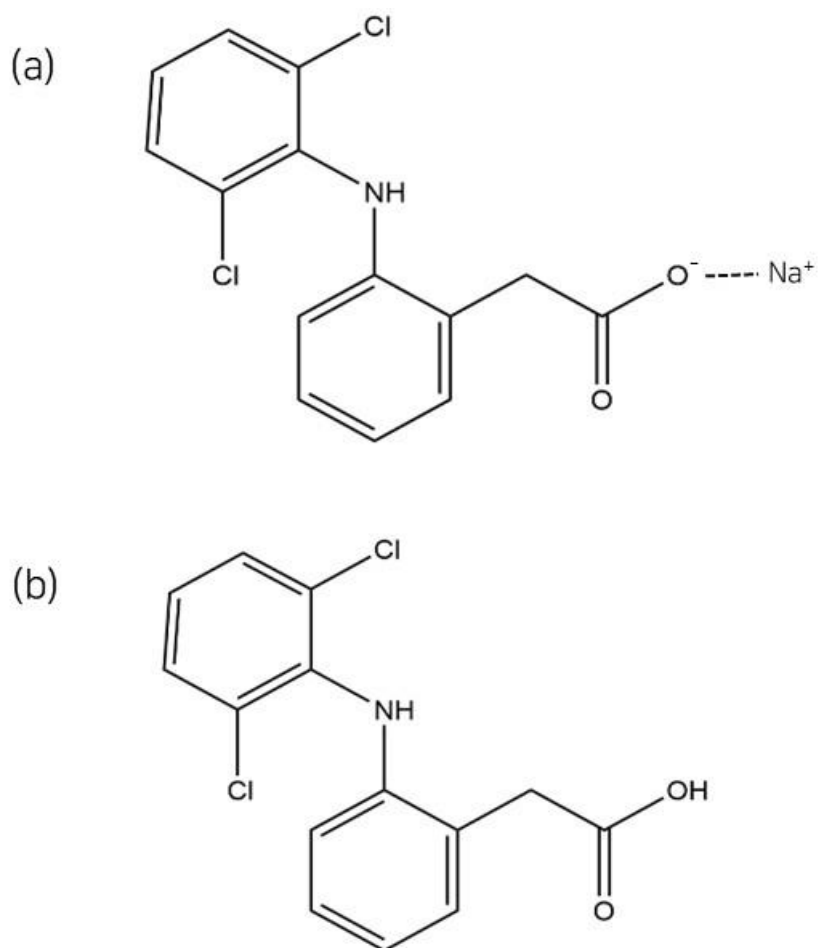


Fig. 2. Chemical structure of Diclofenac sodium (DCF): (a) before dissolving in water; (b) undissociated soluble form and/or undissociated precipitated form

1.1.3. Multi-parameter model

In the application of the MOF-based adsorbents for removal of contaminants, multi-parameter modeling approaches such as response surface methodology (RSM) and artificial neural network (ANN) can be used to predict and optimize the adsorption process.

RSM is a mathematical and statistical technique that is employed to model the effects of various input parameters and their interactions on the output variable and to obtain optimal conditions for the response variable (Jahed Armaghani et al., 2014; Apostolopoulou et al., 2020). In the RSM approach, a parametric model is developed based on the polynomial equation to optimize the adsorption process variables and to predict the target response (Sharma et al., 2015; Sharafi et al, 2019; Samadi-Maybodi et al., 2020).

ANN is a modeling technique that imitates the human neural system to process self-learning. The ANN architecture is composed of input layer, hidden layer, and output layer and small intelligent computational units called 'neuron' to model the nonlinear complex systems. In the ANN approach, a non-parametric model, which is expressed with

transfer functions in hidden layer and output layer respectively, weights, and biases, is developed for prediction of the adsorption process (Esfandiari et al., 2017; Gadekar et al., 2019).

In this study, based on the results of single-parameter experiments and multi-parameter experiments for the adsorption of RhB and DCF by MIL-100(Fe), multi-parameter models, RSM and ANN, were used to predict and optimize for the RhB and DCF adsorption process.

1. 2. Objective

The objective of this study is to investigate adsorption of organic contaminants, RhB and DCF, from aqueous solution using a MIL-100(Fe).

The MIL-100(Fe) was synthesized at room temperature for simpler synthesis process and higher yield than hydrothermal synthesized MOF. The synthesized MIL-100(Fe) at room temperature was conducted various characterizations to analyze physical and chemical properties.

Batch experiments were conducted to investigate adsorption of RhB and DCF from aqueous solution under single-parameter experimental and multi-parameter experimental conditions. Further, multi-parameter modeling was conducted through response surface methodology (RSM) and artificial neural network (ANN). Using the modeled RSM and ANN, the removal rate was predicted within the range of conditions, the factor having the greatest influence for adsorption was predicted, and the optimum condition showing the highest removal rate was derived.

2. Literature Review

2.1. Adsorption of contaminants from aqueous solution using MOFs

Water-stable MOFs have been applied for contaminant removal from aqueous solutions as an adsorbent. Some researchers have synthesized water stable MOF-based composites with carbon nanotubes, graphene, and metal nanoparticles for application to water and wastewater treatment (Torad et al., 2014; Aslam et al., 2017; Liu et al., 2018; Mahmoodi et al., 2019).

Cai et al. (2016) has performed selective adsorption of arsenate using MIL-100(Fe) and adsorption-desorption recycling three times, which has remaining 86% adsorption efficiency. Nasrollahpour et al. (2017) has conducted hexavalent chromium removal from water by Ag based MOFs. The adsorbents are MIL-100(Fe), Fe₃O₄@MIL-100(Fe), and IL-MIL-100(Fe), which is used acidic chloroaluminate (IL) in this study. Fang et al. (2018) has performed adsorption of chromium by MIL-100(Fe), which is introduced by Na₂CO₃ as mineralizing agent and shows improved qualities and higher adsorption capacity than the

precursor, MIL-100(Fe). Georgiou et al. (2018) has performed adsorption of arsenite using MIL-100(Fe) with calcinated at 600, 800, and 900 °C and comparison with other As adsorption Fe/carbon materials. Nehra et al. (2019) has conducted adsorption of phosphate using MIL-100(Fe), which is synthesized with the agents, ammonium molybdate and N,N-Dimethylformamide (DMF). Vo et al. (2019) has performed CO selective adsorption with Cu-doped MIL-100(Fe). Although MIL-100(Fe) adsorbed CO₂ better than CO, Cu-doped MIL-100(Fe) showed selective CO adsorption compared to CO₂ due to π complexation between CO and Cu. Zhang et al. (2019(1)) has performed Pb removal from water using modified MIL-100(Fe), ED-MIL-100(Fe) and conducted comparison of using or not fulvic acid (FA). Zhang et al. (2019(2)) has conducted removal of antimonite and antimonate from water using five Fe-based MOFs, which are Fe-BTC, MIL-100(Fe), MIL-101(Fe), MIL-53(Fe), and MIL-88C(Fe).

Table 1 . Studies for contaminants adsorption from aqueous solutions using MOFs

Reference	Type of MOF	Type of contaminant	Maximum adsorption capacity (mg g ⁻¹)
Cai et al. (2016)	MIL-100(Fe)	Arsenate (As)	27.0
Nasrollahpour et al. (2017)	Ag-MOF	Chromium (Cr)	285.7
Fang et al. (2018)	MIL-100(Fe)	Chromium (Cr)	46.0
Georgiou et al. (2018)	MIL-100(Fe)	Arsenite (As)	120.0
Nehra et al. (2019)	MIL-100(Fe)	Phosphate	93.6
Vo et al. (2019)	Cu-doped MIL-100(Fe)	CO	86.8
Zhang et al. (2019)	ED-MIL-100(Fe)	Lead (Pb)	378.8
Zhang et al. (2019)	MIL-101(Fe)	Antimonate (Sb)	472.8

2.2. Dye adsorption using MOFs

MOF-based adsorbents have been tested for the removal of various organic dyes, including methyl orange, methylene blue, methyl red, rhodamine 6G, rhodamine B, crystal violet, and acid orange 10 in aqueous solutions (Haque et al., 2011; Huo et al., 2012; Tan et al., 2015; Zhao et al., 2015; Ayati et al., 2016; Duan et al., 2016; Liu et al., 2016; Yilmaz et al., 2016; Zhu et al., 2016; Abbasi et al., 2017; Aslam et al., 2017; Fan et al., 2018; Wei et al., 2018). These studies confirmed that MOFs synthesized by hydrothermal synthesis method are effective porous crystallized adsorbents for removing dyes from water.

Duan et al. (2016) has performed comparison of adsorption properties of rhodamine 6G (R6G), RhB, and Reactive red 120 (RR 120) dyes from aqueous solution using a nanoscale material MIL-100(Fe) (NMIL-100(Fe)), which is synthesized at 140 °C and has 3.94 nm of average pore diameter. Liu et al. (2016) has performed adsorptive removal of RhB from aqueous solution by a magnetic MIL-100(Fe) (Fe₃O₄/MIL-100(Fe)), which is synthesized at 200 °C by mixing ferric chloride, sodium acetate, and ethylene glycol in prepared MIL-100(Fe). Yang et al. (2016) has conducted adsorption of RhB using a MIL-68(In)-

NH₂/graphite oxide (GO) composites (In-MOF@GO), which is synthesized using Indium and dispersing GO powder in a well-dissolved indium nitrate/BDC-NH₂ mixture. Jin et al. (2018) has performed comparison of adsorption efficiency of malachite green (MG), congo red (CR), rhodamine b (RhB), methylene blue (MB) and methyl orange (MO) from aqueous solution by MOF-based adsorbent. In this study, nickel (Ni) nanoparticles encapsulated in porous carbon/carbon nanotube hybrids (Ni/PC-CNT) with Ni/Zn-MOF precursor was used as an adsorbent, which has magnetic properties. Zhang et al. (2018) has conducted rapid and selectively adsorption of cationic dyes such as MB, crystal violet (CV), RhB in a mixed solution of positively, neutral (phenol red (PR)), and negatively-charged (MO) dyes. In this study, Zn-MOF with decorated pore surface was used for selectively adsorption of dye from aqueous solution. Cui et al. (2019) has synthesized gel-like Zr-MOF(bpy) and ZnO/Zr-MOF(bpy) nanocomposite for adsorption of RhB from aqueous solution. ZnO/Zr-MOF has high adsorption capacity of 462.3 mg g⁻¹ on RhB adsorption and high surface area of 2141.188 m² g⁻¹. Li et al. (2019) has performed adsorption and catalytic degradation of RhB from water by cal-ZIF67/AC. Cal-ZIF67/AC was made using ZIF-67

loaded onto commercial activated carbon (AC) pellets and calcined at 800 °C. Further, it showed high activity in effective activation of peroxymonosulfate (PMS) to produce sulfate radicals for oxidative degradation of RhB. Jarrah et al. (2020) has performed adsorption of cationic dyes such as RhB and MB from aqueous solution using encapsulation of $K_6P_2W_{18}O_{62}$ into magnetic nanoporous $Fe_3O_4/MIL-101(Fe)$, which has magnetic properties and has high stability, recoverability. Navarathna et al. (2020) has used MIL-53(Fe)/magnetic and magnetite/biochar composites (MOF-MBC) as adsorbent and photocatalyst for RhB removal. These studies confirmed that MOFs synthesized by hydrothermal synthesis method were effective adsorbents for removing dyes in water, but they were limited to calculating the maximum adsorption capacity of adsorbents.

Table 2 . Studies for dye adsorption from aqueous solutions using MOFs synthesized by hydrothermal method

Reference	Type of MOF	Type of dye	Maximum adsorption capacity (mg g ⁻¹)	Initial concentration of dye (mg L ⁻¹)
Duan et al. (2016)	NMIL-100(Fe)	RhB	76.69	-
Liu et al. (2016)	Fe ₃ O ₄ /MIL-100(Fe)	RhB	28.36	0-400
Yang et al. (2016)	MIL-68(In)-NH ₂ /graphite oxide(GO) composites	RhB	267	2-200
Yilmaz et al. (2016)	MIL-53(Fe)	Methyl red	183.5	25-400
Zhu et al. (2016)	MIL-101(Fe)	Methylene blue	473.7	1-40
Aslam et al. (2017)	Fe ₃ O ₄ @MIL-100(Fe)	Methylene blue	221	20-400

Fan et al. (2018)	Fe ₃ O ₄ @MIL-100(Fe)	AO10	39.7	25-50
Jin et al. (2018)	Ni/PC-CNT (Ni/Zn-MOF)	RhB	395	20-350
Wei et al. (2018)	Fe-MOFs	Congo red, Orange II	95.98%, 99.57% (removal rate)	-
Zhang et al. (2018)	Zn-MOF	RhB	3.75	2-20
Cui et al. (2019)	ZnO/Zr-MOF(bpy)	RhB	918.9	10-50
Li et al. (2019)	Cal-ZIF-67/AC	RhB	46.2	-
Jarrah et al. (2020)	P ₂ W ₁₈ O ₆₂ @Fe ₃ O ₄ /MIL-101(Fe)	RhB	68.49	25-250
Navarathna et al. (2020)	MIL-53(Fe)/Magnetite bochar composites	RhB	55	5-1000

2.3. Pharmaceutical adsorption using MOFs

Several researchers have applied MOFs, functionalized MOFs, and/or MOF-based composites as adsorbents for removal of DCF from aqueous solutions (Bhadra et al., 2017; Luo et al., 2018; Li et al., 2019; Zhuang et al., 2019a, b; Karami et al., 2020; Miao et al., 2020; Tran et al., 2020). Hasan et al. (2016) has performed DCF adsorptive removal from water by Zr-based MOF. In this study, UiO-66(Zr) and functionalized UiO-66s (with $\text{SO}_3\text{H}/\text{NH}_2$) were applied in the adsorption and compared to AC. Bhadra et al. (2017) has performed adsorptive removal of ibuprofen (IBP) and DCF from water using MOF-derived porous carbon prepared at $1000\text{ }^\circ\text{C}$ (PCDM-1000). Further, comparisons of IBP and DCF adsorptive removal with PCDM-1000, ZIF-8, and activate carbon (AC) were conducted in this study. Luo et al. (2018) has investigated the adsorption ability of a porous Cu-based MOF for chlorpromazine hydrochloride (CLF) and DCF. The porous Cu-based MOF based on a pentacarboxylate ligand 2,5-bis-benzoic acid (H_5L) has been selected as a adsorbent. Zheng et al. (2018) fabricated $\text{Fe}_3\text{O}_4@\text{MIL-100}(\text{Fe})$ magnetic composites for adsorptive removal of DCF. This $\text{Fe}_3\text{O}_4@\text{MIL-100}(\text{Fe})$ showed a relatively high maximum adsorption capacity of

377.37 mg g⁻¹ compared to its low specific surface area of 198.47 m² g⁻¹. Li et al. (2019) also has used Fe₃O₄@MIL-100(Fe) for aqueous DCF removal through adsorption and photodegradation. The Fe₃O₄@MIL-100(Fe) in this study has high surface area of 1244.62 m² g⁻¹, an excellent maximum adsorption capacity for DCF of 400 mg L⁻¹, and high elimination of TOC (87.8%) was observed during the DCF mineralization process through TOC analyzer. Liu et al. (2019) prepared a copper (Cu)-based MOF (Cu(BTTA)]_n·2DMF) for DCF adsorption. This adsorbent selectively adsorbed to DCF in a mixed solution of DCF, CLF and amodiaquin dihydrochloride (ADQ), and showed a high maximum adsorption capacity of 650 mg g⁻¹. Zhuang et al. (2019) has performed adsorption of DCF using MIL-100(Fe) and theoretically calculated adsorption mechanism through structure simulation using density functional theory (DFT) in quantum chemistry package GAMESS (general atomic and molecular electronic structure system). Karami et al. (2020) has investigated a competitive co-adsorption of naproxen (NAP) and DCF from water using a MIL-53(Al). Single-component experiments for each of NAP and DCF, and binary experiments were performed. The calculated maximum removal

capacities were found to 297 and 422 mg g⁻¹ for NAP and DCF, respectively. Tran et al. (2020) has performed uptake application of Mn₂(BDC)₂(DMF)₂-derived MnO@C nanocomposite for antibiotic contaminants involving tetracycline (TCC), ciprofloxacin (CFX), DCF, and chloramphenicol (CAP) in aqueous solution. Although these studies show that MOFs synthesized by hydrothermal synthesis method are effective adsorbents for the removal pharmaceuticals from water, there is a limitation in that they only calculate the maximum adsorption capacity. Further, DCF has a characteristic of precipitation when the pH is less than 4 - 5, and there was no paper mentioning the precipitation of DCF according to pH among the papers in Table 3. For substances that precipitate in a specific pH range, such as DCF, if modeling is performed through ANN based on adsorption experiments, not only the removal rate due to adsorption but also the removal rate due to precipitation can be considered. Therefore, when fitting the adsorption model equation through a single-parameter adsorption experiment, the experiment should be conducted only under conditions where no precipitation occurs, and a study that can calculate the removal rate considering precipitation through multi-parameter modeling is also required.

Table 3 . Studies for pharmaceutical adsorption from aqueous solutions using MOFs synthesized by hydrothermal method

Reference	Type of MOF	Type of pharmaceutical	Maximum adsorption capacity (mg g ⁻¹)	Initial concentration of pharmaceutical (mg L ⁻¹)	Initial pH
Hasan et al. (2016)	UiO-66(Zr)	Diclofenac	189	-	5.4
Moradi et al. (2016)	Fe ₃ O ₄ @MIL-100(Fe)	Ciprofloxacin	322.6	50-250	6.0
Bayazit et al. (2017)	MIL-101(Cr)	Ciprofloxacin	63.3	5-35	-
Bhadra et al. (2017)	PCDM-1000(Zn)	Diclofenac	400	25-100	-

Chen et al. (2017)	UiO-66(Zr)	Tetracycline	46.4	10-100	-
Li et al. (2017)	ZIF-8	Ciprofloxacin	416.7	3-100	6.0
Naeimi et al. (2017)	MIL-53(Fe)	Doxycycline	322	-	-
Gadipelly et al. (2018)	MOF-5(Zn)	Ciprofloxacin	98.2	10-250	-
Luo et al. (2018)	Cu-MOF	Diclofenac	490	500-1300	7.0
Mirsoleimani et al. (2018)	MOF-5(Zn)	Tetracycline	233	35-75	7.0
Xiong et al. (2018)	MIL-53(Fe)	Tetracycline	364.4	1-200	-
Zheng et al. (2018)	Fe ₃ O ₄ @MIL-100(Fe)	Diclofenac	377.4	20-140	-

Li et al. (2019)	Fe ₃ O ₄ @MIL-100(Fe)	Diclofenac	400	60-140	6.2
Liu et al. (2019)	Cu-MOF	Diclofenac	650	100-1600	-
Sun et al. (2019)	UiO-66(Zr)	Ibuprofen, Naproxen	111.4, 72.5	-	-
Xiong et al. (2019)	MIL-53(Fe)	Doxycycline	397.2	5-150	-
Zhuang et al. (2019)	MIL-100(Fe)	Diclofenac	1021	60-400	6.0
Karami et al. (2020)	MIL-53(Al)	Diclofenac	422	5-600	-
Olawale et al. (2020)	[Cu(Glu) ₂ (H ₂ O ₂)]H ₂ O- MOF	Ciprofloxacin	61.4	5-30	-

Tran et al. (2020)	Mn ₂ (BDC) ₂ (DMF) ₂ - derived MnO@C	Diclofenac	92.4	10-40	-
--------------------	--	------------	------	-------	---

3. Materials and Methods

3.1. Synthesis of MIL-100(Fe) at room temperature

Iron(II) chloride tetrahydrate ($\text{FeCl}_2 \cdot 4\text{H}_2\text{O}$, 99%) and trimesic acid (H_3BTC , 95%) were purchased from Sigma-Aldrich (Saint Louis, MO, USA). Sodium hydroxide (NaOH) and ethyl alcohol ($\text{C}_2\text{H}_5\text{OH}$, 94.5%) were obtained from Duksan Pure Chemicals (Ansan, Republic of Korea) and Daejung Chemicals & Metals (Siheung, Republic of Korea), respectively. The ultrapure water was purified by a Milipore Milli-Q water purification system.

The MIL-100(Fe) was synthesized at room temperature following the procedures described in Guesh et al. (2017) and Fig. 3. First, NaOH (24.0 mM) and H_3BTC (8.0 mM) were dissolved in 30 mL of deionized water (DW) (solution (①)). Second, $\text{FeCl}_2 \cdot 4\text{H}_2\text{O}$ (12.07 mM) was dissolved in 96 mL of DW (solution (②)). Solution (①) was added dropwise to solution (②), stirred for 24 h at room temperature, and centrifuged at 4000 rpm to obtain the solid product. Then, the solid was washed several times with DW and ethyl alcohol, and dried overnight at 90°C in a vacuum drying oven (SH-VDO-08NG, Samheung, Seoul,

Republic of Korea) to obtain the final MIL-100(Fe) product. MOF synthesized at room temperature has the advantage that it requires fewer instruments and has a much simpler synthesis process than the hydrothermal synthesis method used in previous studies.

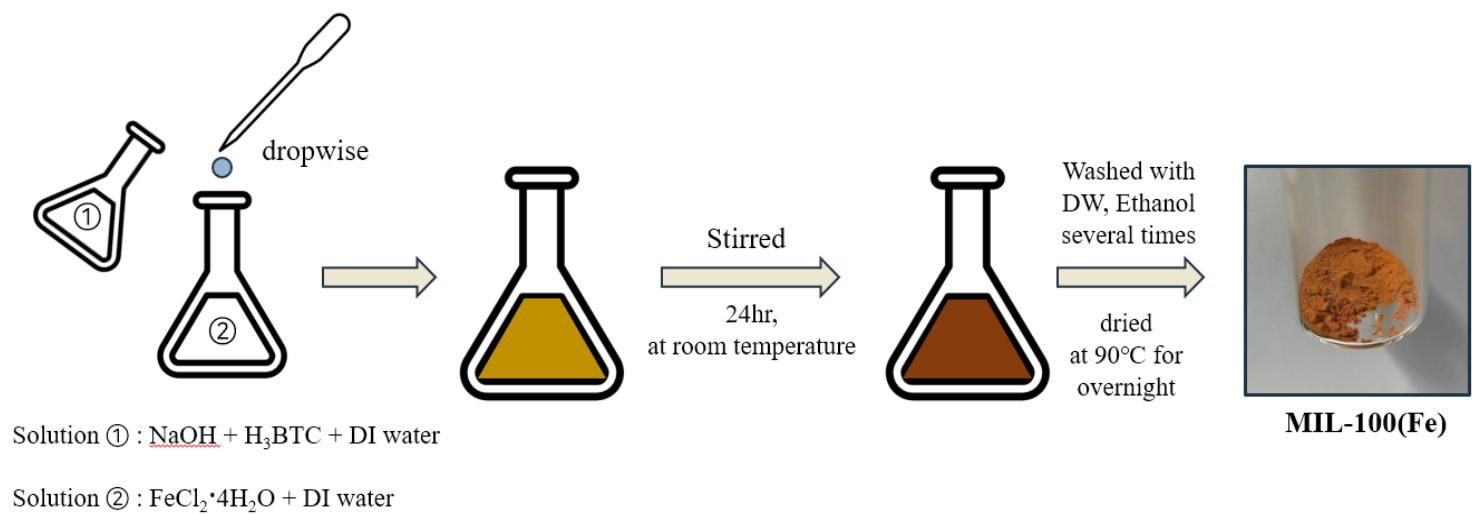


Fig. 3. A schematic diagram of the MIL-100(Fe) synthesis process at room temperature

3.2. Characterization of MIL-100(Fe)

Several instruments were used to analyze the physical and chemical characteristics of the MIL-100(Fe). A field emission scanning electron microscope (FESEM, Supra 55VP, Carl Zeiss, Oberkochen, Germany) was employed to examine the surface morphology. Furthermore, an energy dispersive X-ray spectroscopy (EDS) pattern was determined using FESEM to confirm the constituent elements of adsorbent and their ratio. The X-ray diffraction (XRD) pattern was obtained using powder X-ray diffractometry (D8 Advance, Bruker, Billerica, MA, USA) with the 2θ range from 2° to 20° . An electrophoretic light scattering (ELS) spectrophotometer (ELSZ-1000, Otsuka Electronics, Tokyo, Japan) was employed to measure the zeta potential and particle diameter. Nitrogen gas (N_2) adsorption-desorption analysis was conducted using a surface area analyzer (BELSORP-MAX, MicrotracBEL, Osaka, Japan) to determine the Brunauer-Emmett-Teller (BET) surface area, average pore diameter and total pore volume. A thermogravimetric analyzer (Discovery TGA, TA Instruments, New Castle, DE, USA) was used for thermogravimetric analysis (TGA) by heating the MIL-100(Fe) to 800°C with a heating rate of $10^\circ\text{C min}^{-1}$. The changes of components before and after adsorption experiments were obtained using X-ray photoelectron spectrometer (XPS,

AXIS SUPRA, Kratos Analytical Inc., Manchester, U.K). Furthermore, Fourier-transform infrared (FTIR) spectra was determined using a spectrophotometer (Nicolet 6700, Thermo Scientific, Waltham, MA, USA) using KBr pellets for analyzing chemical bonding before and after adsorption processes.

Water stability of the MIL-100(Fe) was analyzed in deionized water (DW) and RhB, DCF solution. The stability tests were performed in duplicate at the solution pHs of 2, 7, and 12. 80 mg of the MIL-100(Fe) was added into 40 mL of DW and RhB, DCF solution (100 mg L^{-1}) in polypropylene conical tubes and stirred in a shaking incubator (Daihan Science, Seoul, Republic of Korea) at 150 rpm and 30 °C for 24 h, respectively. After reaction, the amount of Fe leaching from the MIL-100(Fe) was quantified using Inductively Coupled Plasma-Optical Emission Spectrometry (ICP-OES) (iCAP 7000, Thermo Fisher Scientific, Waltham, MA, USA).

3.3. RhB adsorption from synthetic water

3.3.1. Single-parameter experiments for RhB removal

A Stock solution (200 mg L^{-1}) was prepared by Rhodamine B (Sigma-Aldrich, Saint Louis, MO, USA). Batch adsorption experiments were conducted with polypropylene conical tubes containing 50 mL RhB solution (Initial RhB concentration = 50 mg L^{-1} , Initial pH = 4) and 50 mg MIL-100(Fe) (adsorbent dose = 1.0 g L^{-1}). All batch tests were performed in a shaking incubator (Lab. Companion IS-971R) at 150 rpm and 30°C for 24 h in duplicate. The range of RhB initial concentration was 10 - 100 mg L^{-1} , adsorbent dose was 0.01 - 0.1 g. The pH range of dye solution was 2 - 12 and the temperature range was $20 - 40^\circ\text{C}$ (Table 4.).

After the reaction, the samples were filtered through a $0.45\text{-}\mu\text{m}$ membrane filter. The concentrations of RhB were determined by a UV-Vis spectrophotometer (Genesys 10S, Thermo Scientific, Waltham, MA, USA) at a wavelength of 470 nm based on the calibration curve obtained from the spectra of the RhB standard solutions, and the curve is fitted with a linear fit (Fig. 4.). The equilibrium adsorption capacity was calculated as

$$q_e = \frac{(C_0 - C_e)V}{m}$$

where, q_e (mg g^{-1}) represents the adsorption capacity; C_0 (mg L^{-1}) is the initial RhB concentration; C_e (mg L^{-1}) is the equilibrium RhB concentration; V (L) is the volume of solution; m (g) is the weight of adsorbents. Further, the removal rate (removal efficiency, E (%)) was calculated as

$$E = \frac{(C_0 - C_e)}{C_0} \times 100$$

Table 4. Batch experiment conditions for RhB removal

Experiments \ Conditions	Dosage (g/L)	Contact time (min)	Initial concentration (mg/L)	Temperature (°C)	Initial pH
Equilibrium	1	1440	10, 20, 30, 40, 50, 60, 80, 100	30	4
Kinetic	1	2, 5, 10, 15, 30, 60, 120, 240, 360, 480, 600, 720, 1440	50	30	4
Temperature	1	1440	50	20, 30, 40	4
pH	1	1440	50	30	2, 4, 6, 8, 10, 12

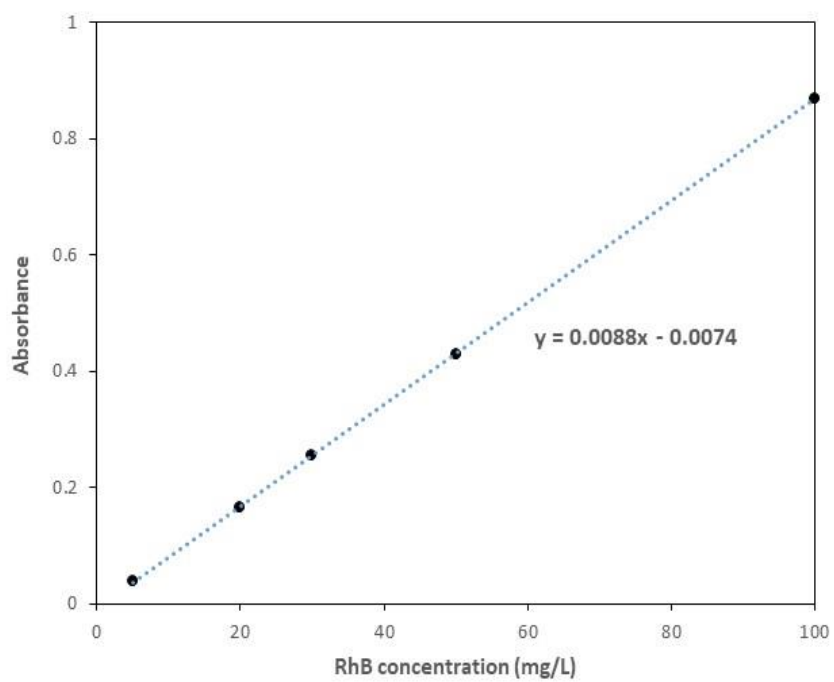


Fig. 4 Calibration curve obtained with RhB standard solutions

3.3.2. Multi-parameter experiments for RhB removal

Multi-parameter experiments for RhB removal were performed based on the single-parameter experiments. The single parameter experiments are performed by changing only one variable, such as dosage, contact time, initial contaminant concentration, temperature, and initial pH, and the multi-parameter experiments are performed by changing several variables at the same time. First, an experimental design was performed using the central composite design (CCD) method. The number of experimental points (N) were calculated using the following formula (Nair et al., 2014):

$$N = 2^k + 2k + cp \quad (13)$$

where, k is the number of input variables, 2^k is the number of factorial points, $2k$ is the number of axial points, and cp is the number of center points. Experimental range and level of input variable for RhB adsorption in the CCD approach are presented in Table 5. In this study, input variables including pH (A), adsorbent dose (B), and initial RhB concentration (C) were chosen as five levels and labeled as -2 to +2 for RhB adsorption. The response parameter was the removal rate of RhB. The range of input variables was determined based on the preliminary adsorption experiments

described in the Section 3.3.1. The CCD matrix in Table 6 was obtained using the Design Expert software (version 12, Stat-Ease, Minneapolis, MN, USA). Based on the CCD matrix, adsorption experiments were conducted in duplicate for each experimental point for RhB (N=30).

Table 5. CCD levels of input variables ($\alpha=2$) for RhB adsorption

Input variable	Unit	Symbol	Levels				
			$-\alpha$	-1	0	+1	$+\alpha$
pH	-	A	2	3	4	5	6
Dosage	g/L	B	1	1.5	2	2.5	3
Initial RhB concentration	mg/L	C	50	75	100	125	150

Table 6. Designed matrix conditions for RhB adsorption

Ex.	Initial pH	MIL-100(Fe) dosage (g/L)	Initial RhB concentration (mg/L)	Experimental point
1	2.0	2.0	100	Axial point
2	4.0	1.0	100	
3	4.0	2.0	50	
4	4.0	2.0	150	
5	4.0	3.0	100	
6	6.0	2.0	100	
7	3.0	1.5	75	Factorial point
8	3.0	1.5	125	
9	3.0	2.5	75	
10	3.0	2.5	125	
11	5.0	1.5	75	
12	5.0	1.5	125	
13	5.0	2.5	75	
14	5.0	2.5	125	
15	4.0	2.0	100	Center point

3.4. DCF adsorption from synthetic water

3.4.1. Single-parameter experiments for DCF removal

A Stock solution (1000 mg L⁻¹) was prepared by Diclofenac sodium (Sigma-Aldrich, Saint Louis, MO, USA). Batch adsorption studies were performed with polypropylene conical tubes containing 50 mL of the DCF solution (Initial DCF concentration = 80 mg L⁻¹, Initial pH = 7) and 10 mg MIL-100(Fe) (adsorbent dose = 0.2 g L⁻¹). All duplicate samples were stirred in a shaking incubator at 150 rpm, 30 °C for 24 h. The range of DCF initial concentration was 20 - 1000 mg L⁻¹, pH range of dye solution was 5 - 12 and the temperature range was 10 - 50 °C (Table 7.).

The designed pH condition is to experiment in a range where DCF does not precipitate. Depending on solution pH, DCF exist as DCF⁻ (dissociated soluble form), DCF-H_(aq) (undissociated soluble form), and/or DCF-H_(s) (undissociated precipitated form) in aqueous solutions. The DCF distribution was calculated based on the following acid-base equilibrium formula:

$$K_a = \frac{[DCF^-][H^+]}{[DCF-H]}, \quad pK_a = -\log(K_a) \quad (1)$$

where, K_a is the acidic dissociation constant (DCF $pK_a = 4.15$). The

solubility of DCF (DCF-H) was calculated based on the following equation:

$$S_H = S_0 \left(1 + \frac{K_a}{[H^+]} \right) \quad (2)$$

where, S_H is the solubility of DCF-H (mg L^{-1}) and S_0 is the intrinsic solubility of DCF-H ($= 2.37 \text{ mg L}^{-1}$). According to the equations, the species distribution of DCF when the total DCF concentration is 80 mg L^{-1} is shown in Fig. 5. As an example, DCF was composed of DCF^- (87.6%), $\text{DCF-H}_{(\text{aq})}$ (12.4%), and $\text{DCF-H}_{(\text{s})}$ (0%) at pH 5.

After the reaction, the samples were filtered through a $0.45\text{-}\mu\text{m}$ membrane filter. The concentrations of DCF were determined by a UV-Vis spectrophotometer at a wavelength of 274 nm based on the calibration curve obtained from the spectra of the DCF standard solutions (Fig. 6.).

Table 7. Batch experiment conditions for DCF removal

Experiments \ Conditions	Dosage (g/L)	Contact time (min)	Initial concentration (mg/L)	Temperature (°C)	Initial pH
Equilibrium	0.2	1440	20, 30, 50, 100, 300, 500, 1000	30	7
Kinetic	0.2	5, 15, 30, 60, 120, 240, 360, 480, 720, 1440	80	30	7
Temperature	0.2	1440	80	10, 20, 30, 40, 50	7
pH	0.2	1440	80	30	5, 6, 8, 10, 12

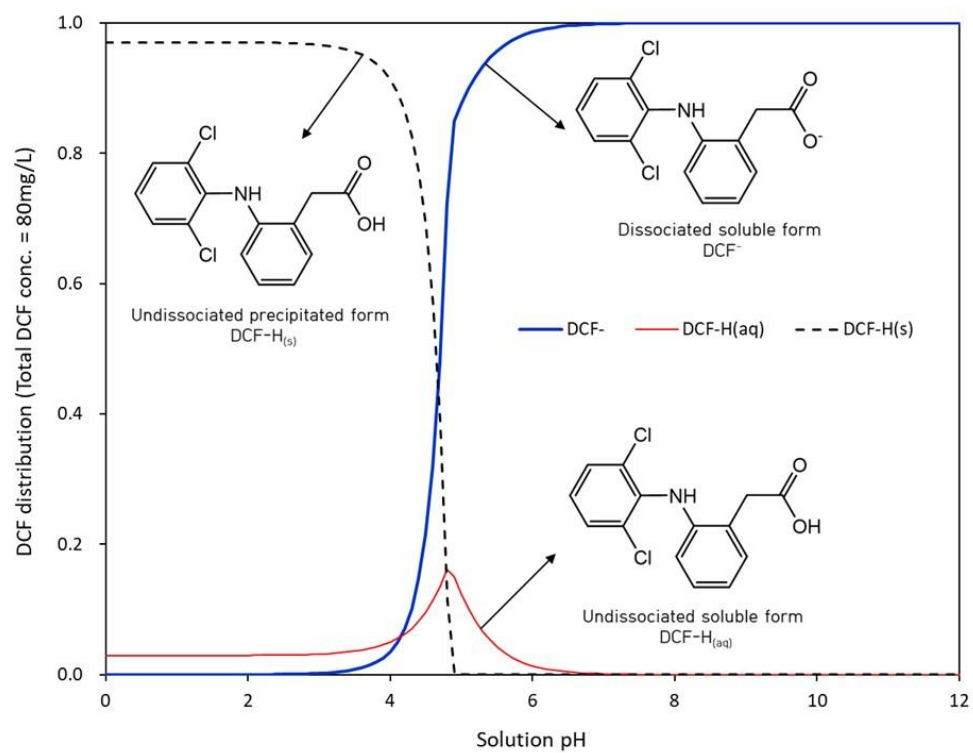


Fig. 5. Species distribution of DCF in response to solution pH at a total DCF concentration of 80 mg L⁻¹

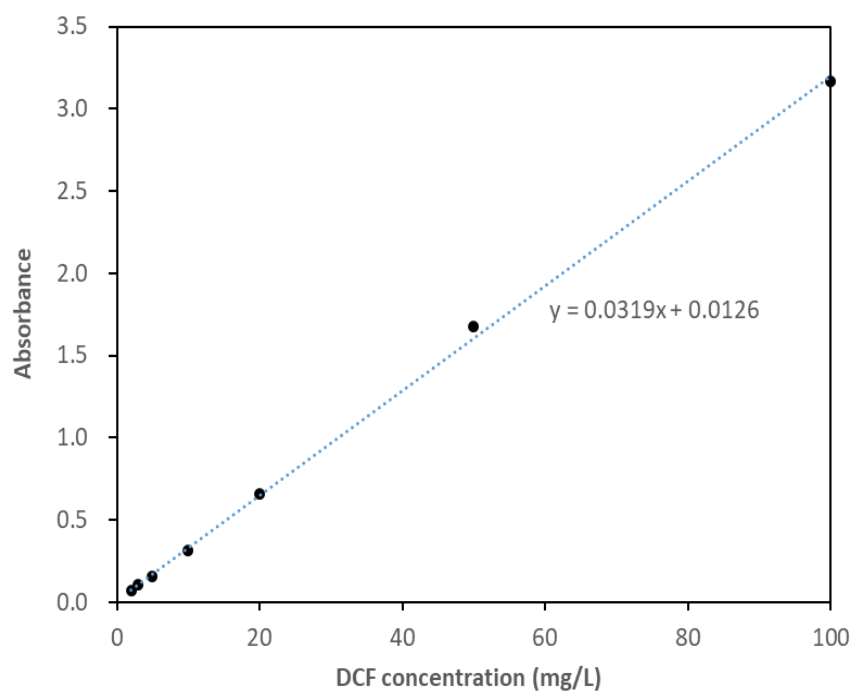


Fig. 6. Calibration curve obtained with DCF standard solutions

3.4.2. Multi-parameter experiments for DCF removal

Multi-parameter experiments for DCF removal were performed based on the single-parameter experiments. An experimental design was performed using the CCD method like RhB removal. Experimental range and level of input variable for DCF adsorption in the CCD approach are presented in Table 8. In this study, input variables including initial pH (A), adsorbent dose (B), and initial DCF concentration (C), and temperature (D) for DCF adsorption were chosen as five levels and labeled as -2 to +2. The response parameter was the removal rate of DCF and final pH. The range of input variables was determined based on the preliminary adsorption experiments described in the Section 3.4.2. The CCD matrix in Table 9 was obtained using the Design Expert software. Based on the CCD matrix, adsorption experiments were conducted in duplicate for each experimental point for DCF (N=56).

Table 8. CCD levels of input variables ($\alpha=2$) for DCF adsorption

Input variable	Unit	Symbol	Levels				
			$-\alpha$	-1	0	+1	$+\alpha$
pH	-	A	5.0	6.5	8.0	9.5	11.0
Dosage	g/L	B	0.4	0.6	0.8	1.0	1.2
Initial RhB concentration	mg/L	C	20	40	60	80	100
Temperature	°C	D	10	20	30	40	50

Table 9. Designed matrix conditions for DCF adsorption

Ex.	Initial pH	MIL-100(Fe) dosage (g/L)	Initial DCF concentration (mg/L)	Temperature (°C)	Experimental point
1	5.0	0.8	60	30	Axial point
2	11.0	0.8	60	30	
3	8.0	0.4	60	30	
4	8.0	1.2	60	30	
5	8.0	0.8	60	10	
6	8.0	0.8	60	50	
7	8.0	0.8	20	30	
8	8.0	0.8	100	30	
9	6.5	0.6	40	20	Factorial point
10	6.5	0.6	80	20	
11	6.5	0.6	40	40	
12	6.5	0.6	80	40	
13	6.5	1.0	40	20	
14	6.5	1.0	80	20	
15	6.5	1.0	40	40	
16	6.5	1.0	80	40	
17	9.5	0.6	40	20	
18	9.5	0.6	80	20	
19	9.5	0.6	40	40	
20	9.5	0.6	80	40	
21	9.5	1.0	40	20	
22	9.5	1.0	80	20	
23	9.5	1.0	40	40	
24	9.5	1.0	80	40	
25	8.0	0.8	60	30	Center point
26	8.0	0.8	60	30	
27	8.0	0.8	60	30	
28	8.0	0.8	60	30	

3.5. Data analysis for single-parameter experiments

After the adsorption studies, the equilibrium data were fitted by the isotherm models of Langmuir, Freundlich and Redlich-Peterson model. The equations of each model can be presented as follows:

$$q_e = \frac{Q_m K_L C_e}{1 + K_L C_e} \quad (3)$$

$$q_e = K_F C_e^{\frac{1}{n}} \quad (4)$$

$$q_e = \frac{K_R C_e}{1 + a_R C_e^g} \quad (5)$$

where q_e indicates the amount of contaminant adsorbed at equilibrium, C_e is the equilibrium concentration of contaminant in the aqueous solution, Q_m is the maximum adsorption capacity, K_L is the Langmuir constant, K_F is the Freundlich constant, $\frac{1}{n}$ is the Freundlich constant related to the adsorption intensity, K_R is the Redlich-Peterson constant, a_R is the Redlich-Peterson constant related to the affinity, and g is the Redlich-Peterson constant related to the adsorption intensity.

The adsorption kinetic data was fitted by Pseudo-first model, Pseudo-

second model and Elovich model. The equations of each model can be presented as follows:

$$q_t = q_e(1 - e^{-k_1 t}) \quad (6)$$

$$q_t = \frac{k_2 q_e^2 t}{1 + k_2 q_e t} \quad (7)$$

$$q_t = \frac{1}{\beta} \ln(\alpha\beta) + \frac{1}{\beta} \ln t \quad (8)$$

where, q_t is the amount of contaminant adsorbed at time t , q_e is the amount of contaminant adsorbed at equilibrium, k_1 is the pseudo first-order rate constant, k_2 is the pseudo second-order rate constant, α is the initial adsorption rate constant, and β is the Elovich adsorption constant.

The coefficient of determination coefficient (R^2), chi-square coefficient (χ^2), and sum of the absolute errors (SAE) were used as error function to analyze the sorption data and fit to the model:

$$R^2 = \frac{\sum_{i=1}^m (y_c - \bar{y}_e)_i^2}{\sum_{i=1}^m (y_c - \bar{y}_e)_i^2 + \sum_{i=1}^m (y_c - y_e)_i^2} \quad (9)$$

$$\chi^2 = \sum_{i=1}^m \left[\frac{(y_e - y_c)^2}{y_c} \right]_i \quad (10)$$

$$\text{SAE} = \sum_{i=1}^m |y_c - y_e|_i \quad (11)$$

where, y_c is the calculated adsorption capacity from the model, and y_e is the measured adsorption capacity from the experiments.

Furthermore, the thermodynamic data were analyzed by the following equations:

$$\Delta G^0 = \Delta H^0 - T\Delta S^0 \quad (12)$$

$$\Delta G^0 = -RT \ln K_e \quad (13)$$

$$\ln K_e = \frac{\Delta S^0}{R} - \frac{\Delta H^0}{RT}; K_e = \frac{aq_e}{C_e} \quad (14)$$

where, ΔG^0 is the change in Gibb's free energy, ΔS^0 is the change in entropy, ΔH^0 is the change in enthalpy, T is the temperature ($^{\circ}\text{C}$), R is the gas constant, and K_e is the equilibrium constant.

3.6. Multi-parameter modeling through RSM and ANN

3.6.1. Response surface methodology (RSM)

RSM was applied to analyze the RhB adsorption data obtained from the designed experiments. The influence of the input variables on the RhB removal rate was modeled by the following cubic polynomial equation (Saldana-Robles et al., 2014; Boudechiche et al., 2017):

$$\begin{aligned} y &= \beta_0 + \sum_{i=1}^k \beta_i x_i + \sum_{i=1}^k \beta_{ii} x_{ii}^2 + \sum_{i=1}^k \beta_{iii} x_{iii}^3 + \sum_{i=1}^{k-1} \sum_{j=i+1}^k \beta_{ij} x_i x_j \\ &+ \sum_{i=1}^{k-2} \sum_{j=i+1}^{k-1} \sum_{k=j+1}^k \beta_{ijk} x_i x_j x_k + \epsilon \end{aligned} \quad (15)$$

where, y is the output value (RhB removal rate), x_i, x_j , and x_k are the input variables, $\beta_0, \beta_i, \beta_{ii}$, and β_{iii} are the regression coefficients for intercept, linear, quadratic, and cubic term, respectively, β_{ij} and β_{ijk} are the cross-product term coefficients, ϵ is the error associated with the adsorption experiments, and k is the number of input variables (= 3). For the RSM modeling, the input variables were normalized in the range of -1 to

1 to avoid the scaling effect using the following equation:

$$x_n = 2 \times \frac{(x - x_{min})}{(x_{max} - x_{min})} - 1 \quad (16)$$

where, x is the input value, x_{min} is the minimum value of x , x_{max} is the maximum value of x . The RSM model was developed based on equation (15) using the Design Expert software. The analysis of variance (ANOVA) test was performed to evaluate the fitness of the developed RSM model to the RhB adsorption data based on the fisher value (F -value), probability value (P -value), and coefficient of determination value (R^2):

$$R^2 = 1 - \frac{\sum_{i=1}^N (y_{i,pre} - y_{i,obs})^2}{\sum_{i=1}^N (y_{i,obs} - y_{ave})^2} \quad (17)$$

where, $y_{i,pre}$, $y_{i,obs}$, and y_{ave} are the predicted value, observed value, and average value of RhB removal rate, respectively.

3.6.2. Artificial neural network (ANN)

ANN was used to modeling for the RhB and DCF adsorption data from the designed experiments. The ANN architecture for the RhB and DCF adsorption is illustrated in Fig. 8. The ANN model was composed of three layers (input, hidden, and output layers). The input layer could include various input variables like pH, adsorbent dose, initial contaminant concentration, temperature, whereas the hidden and output layers could contain a number of neurons for each layer (Jahed Armaghani et al., 2017; Mahmoodi et al., 2019). For the ANN modeling, the input variables were also normalized in the range of -1 to 1.

The effect of the input variables (A, B, C etc.) on the RhB or DCF removal rate and final pH for DCF adsorption (y) were modeled by the following formula (Ghaedi et al., 2015; Baziar et al., 2017):

$$y = \text{Purelin} \left[\mathbf{w}_O \times \text{Tansig} \left(\mathbf{w}_H \times \begin{bmatrix} A \\ B \\ C \end{bmatrix} + \mathbf{b}_H \right) + \mathbf{b}_O \right] \quad (18)$$

where, \mathbf{w}_H and \mathbf{w}_O are the weight values of hidden layer and output layer, respectively, and \mathbf{b}_H and \mathbf{b}_O are the bias values of hidden layer and output layer, respectively. The hyperbolic tangent sigmoid transfer function (Tansig)

was used as a transfer function for the hidden layer, whereas the linear transfer function (Purelin) was used for the output layer. The ANN model was developed based on equation (18) using the MATLAB nntool (R2019b, MathWorks, Natick, MA, USA). The mean squared error (MSE) was used as an error function:

$$\text{MSE} = \frac{1}{N} \sum_{i=1}^N (|y_{i,pre} - y_{i,obs}|)^2 \quad (19)$$

The Levenberg-Marquardt algorithm was selected for the modeling process because it could result in the smaller MSE value (Baziar et al., 2017). In the ANN model development, a total data points ($N = 30$ for RhB, and $N = 56$ for DCF) were randomly divided into three subsets including training set (60%), validating set (20%), and testing set (20%). In the training phase, 60% of data points were used to adjust the weight and bias values for reducing the error between the observed outputs and the predicted outputs (Ghaedi et al., 2017; Gadekar et al., 2019). In the validating phase, 20% of data points were used to prevent overfitting (Ma et al., 2019). In the testing phase, the remaining 20% of data points were used to evaluate the fitness of the developed ANN model to the experimental data.

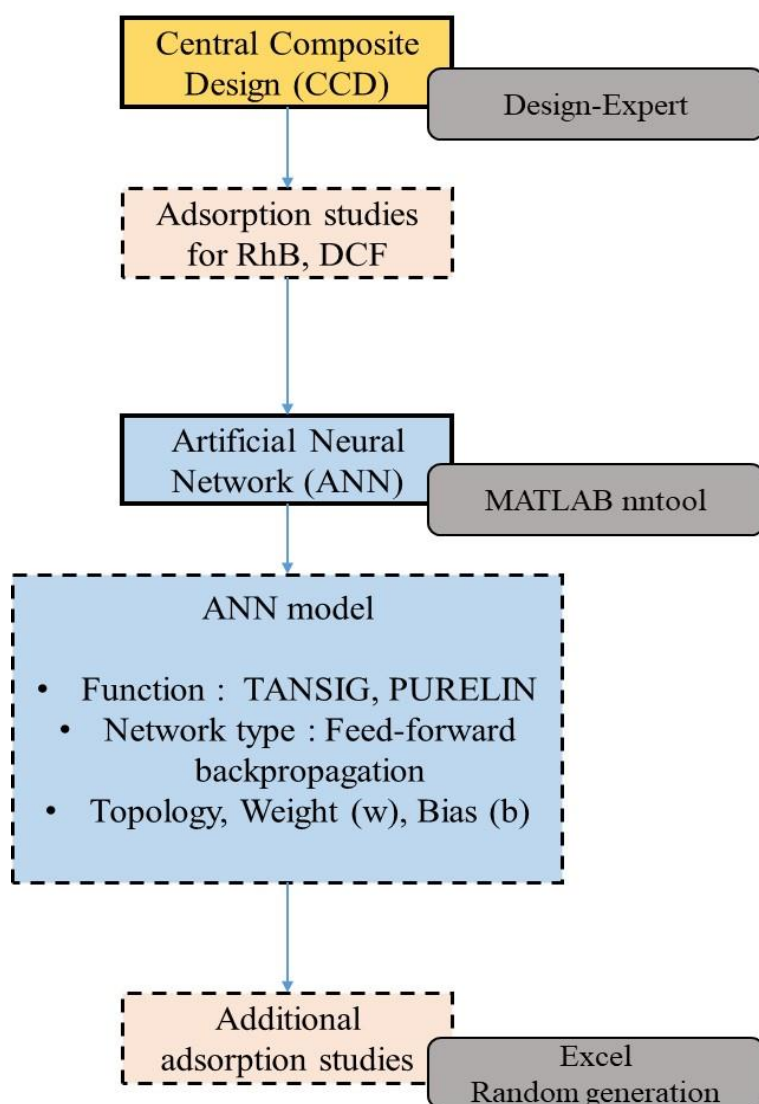


Fig. 7. Schematic diagram of experimental design and modeling analysis with the tools

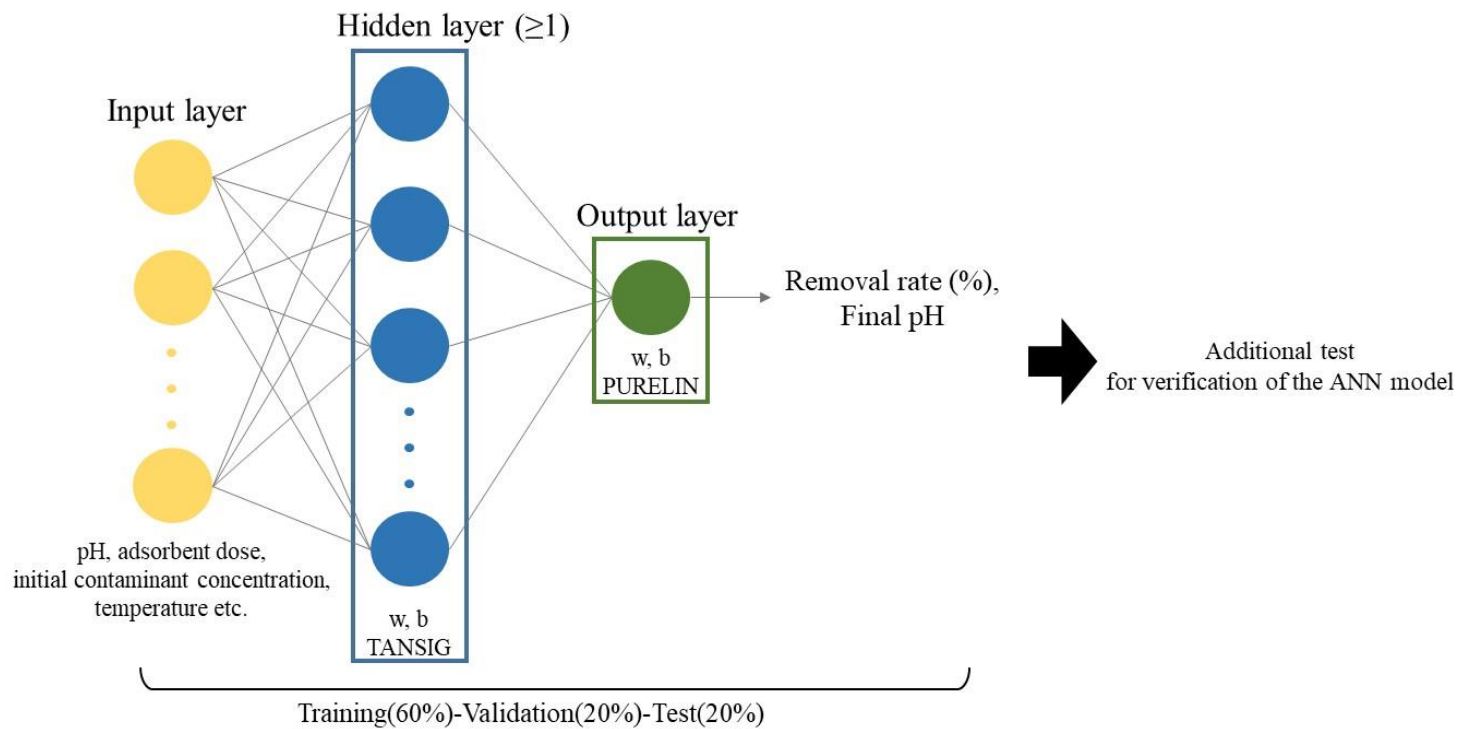


Fig. 8. Artificial neural network (ANN) architecture

4. Results and Discussion

4.1. Characterization of MIL-100(Fe)

FESEM images of MIL-100(Fe) according to various pH are shown in Fig. 9. The synthesized MIL-100(Fe) has an octahedral shape as shown in the Fig. 9, except for (f) at pH 12. At pH 12, much of the MIL-100(Fe)'s crystalline structure has collapsed. The EDS spectra is presented in Fig. 10. The MIL-100(Fe) consists of carbon (C), oxygen (O), and iron (Fe) with the weight percentages of 47.3%, 34.6%, 18.1%, respectively.

The XRD pattern of the MIL-100(Fe) is shown in Fig. 11. In the XRD pattern for all pH ranges, the diffraction peaks centered at 3.4° , 4.0° , 4.8° , 6.3° , 11.0° can be indexed to the (022), (113), (004), (333), and (428) planes of crystallized MIL-100(Fe), respectively. Comparing with MIL-100(Fe)-RT 24h in the previous study (Guesh et al., 2017), which was synthesized at room temperature, it was confirmed that the characteristic peaks of MIL-100(Fe) coincide.

The ELS spectra of the MIL-100(Fe) with pH 2 to 12 is presented in Fig. 12. According to the Fig. 12, a point of zero charge (pH_{pzc}) of MIL-100(Fe) is 4.2. Furthermore, the MIL-100(Fe) had an average hydrodynamic diameter

of $4.3 \pm 0.9 \mu\text{m}$. N_2 adsorption-desorption analysis gave $1752.2 \text{ m}^2 \text{ g}^{-1}$ for BET surface area, 1.67 nm for average pore diameter, and $0.73 \text{ cm}^3 \text{ g}^{-1}$ for total pore volume of MIL-100(Fe) (Fig. 13.).

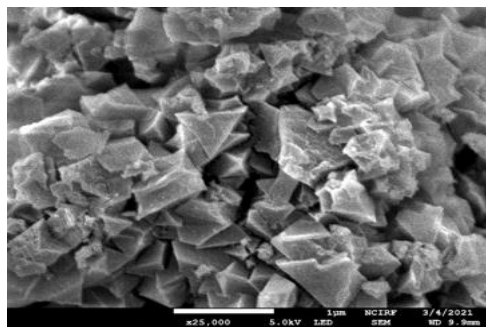
As shown in Fig. 14, MIL-100(Fe) has three distinct weight losses in the range of $20 - 500 \text{ }^\circ\text{C}$ according to the TGA analysis. The first weight loss (15.1%) result from the loss of the water molecules from pores of the MIL-100(Fe) in the range from 20 to $85 \text{ }^\circ\text{C}$. The second weight loss (15.4%) result from the evaporation of the water molecules in the $85 - 360 \text{ }^\circ\text{C}$ range. The final weight loss (44.7%) result from the combustion of the organic linker, trimesic acid, and collapsing of the MIL-100(Fe) framework in the range of $360 - 500 \text{ }^\circ\text{C}$. The TGA curve indicates that the MIL-100(Fe) has thermal stability up to $360 \text{ }^\circ\text{C}$.

The XPS spectra of the MIL-100(Fe) is presented in Fig. 15. In the wide scan (Fig. 15a), the peaks of Fe 2p (711.3 eV), O 1s (531.3 eV), and C 1s (284.3 eV) indicated the structural analogs of the MIL-100(Fe) structure. The high-resolution scan of C 1s (Fig. 15b) showed two peaks assigned to a benzene ring (284.3 eV) and carboxyl group (288.6 eV).

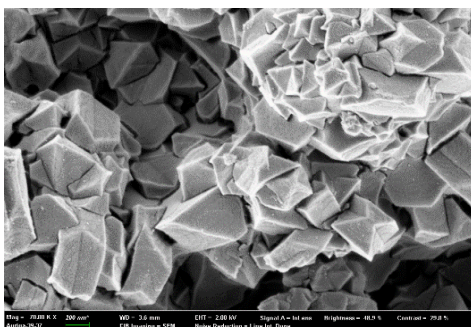
In the FT-IR spectra of the MIL-100(Fe) (Fig. 16.), 2972 cm^{-1} peak corresponded to the O-H stretching (Mohammadifard et al., 2019), 1700 cm^{-1}

and 1620 cm^{-1} peaks corresponded to the C=O stretching (Duan et al., 2016; Lee et al., 2017; Mohammadifard et al., 2019). 1365 cm^{-1} peak corresponded to the C=C bond, 759 cm^{-1} and 708 cm^{-1} peaks corresponded to the Fe-OH vibration (Lee et al., 2017; Mohammadifard et al., 2019).

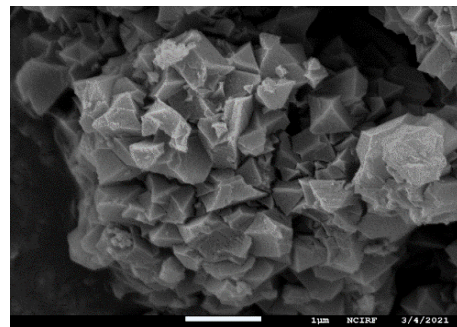
The Water stability of the MIL-100(Fe) in DW, RhB, and DCF solutions are presented in Table 10. A negligible amount of Fe ions were leached from the MIL-100(Fe) during the reaction, indicating that the MIL-100(Fe) had great water stability.



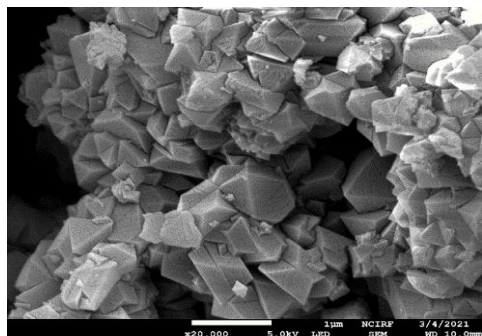
(a) pH 2



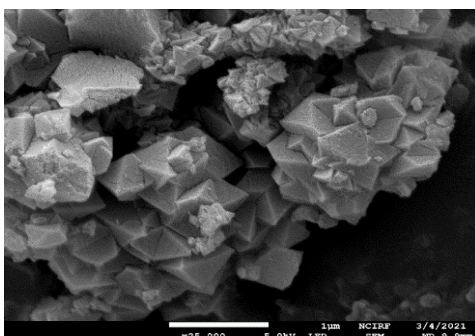
(b) pH 4



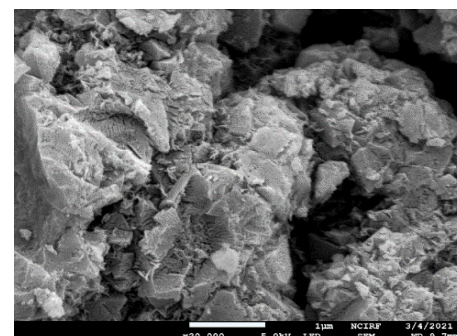
(c) pH 6



(d) pH 8



(e) pH 10



(f) pH 12

Fig. 9. FESEM images of MIL-100(Fe) according to various pH: (a) at pH2; (b) pH4; (c) pH6; (d) pH8; (e) pH10; (f) pH12

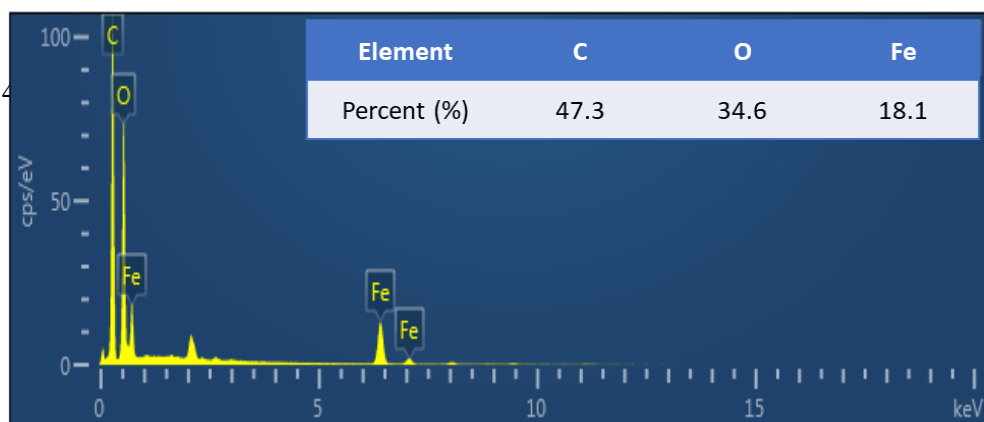


Fig. 10. EDS spectra of the MIL-100(Fe)

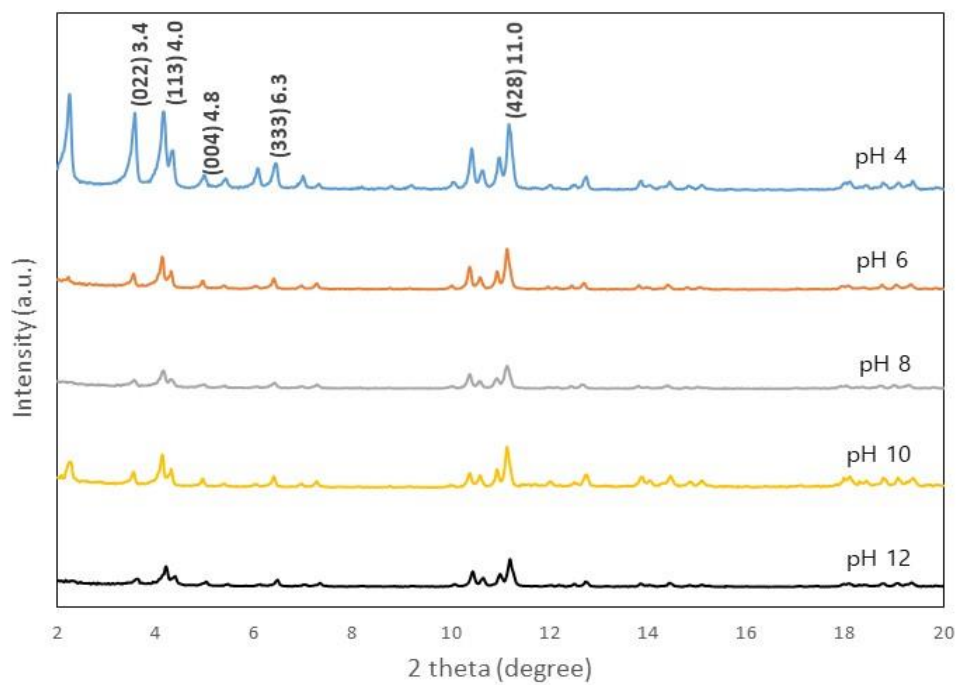


Fig. 11. XRD pattern of the MIL-100(Fe) with various pH

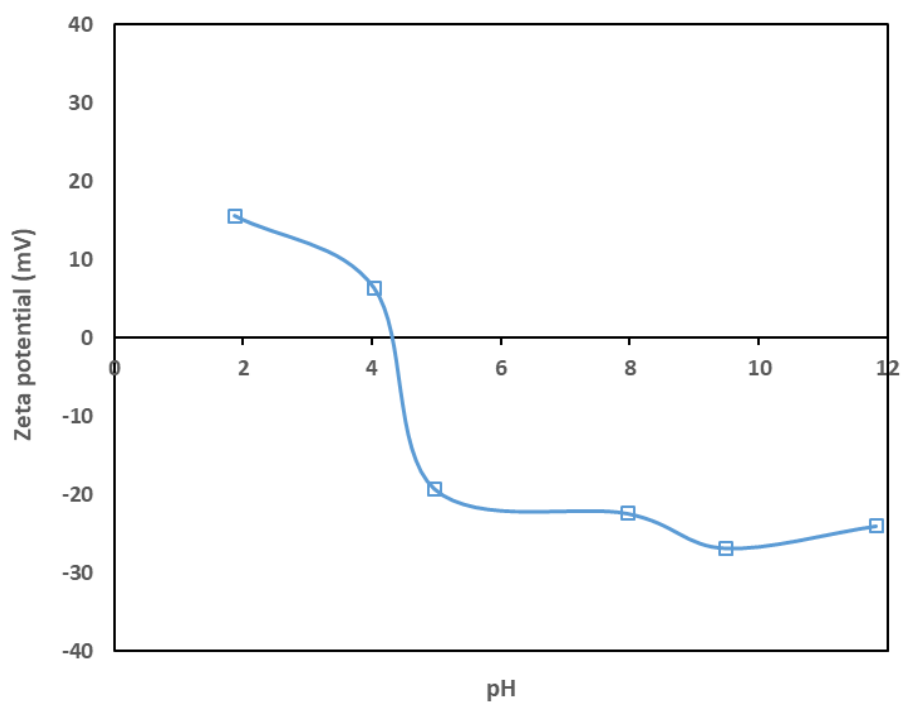


Fig. 12. ELS spectra (zeta potential) of the MIL-100(Fe)

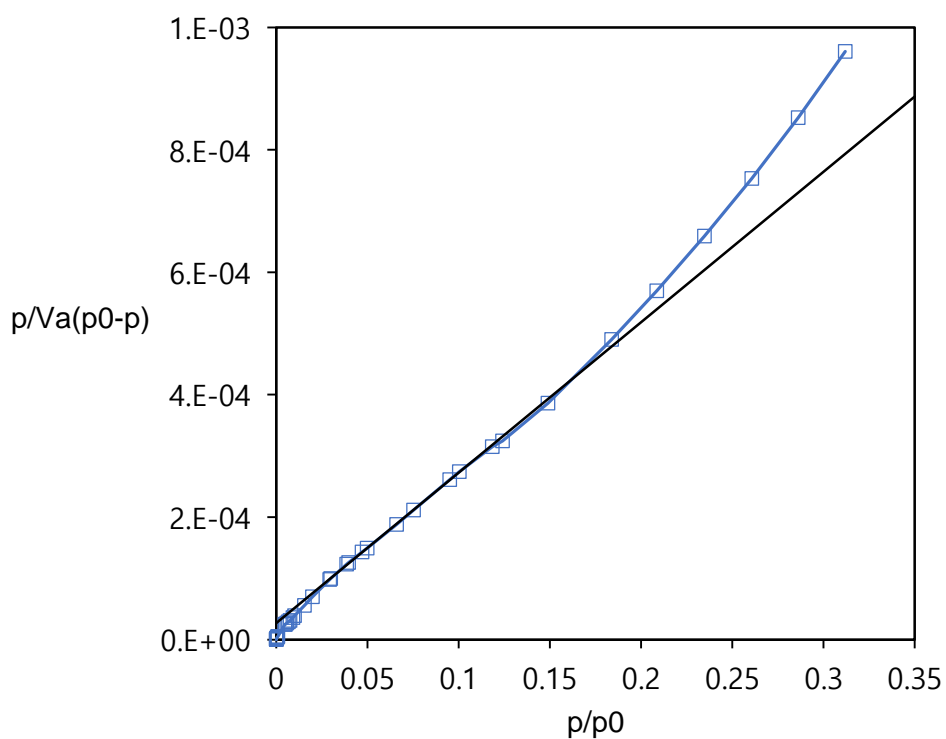


Fig. 13. N₂ adsorption-desorption isotherms of the MIL-100(Fe)

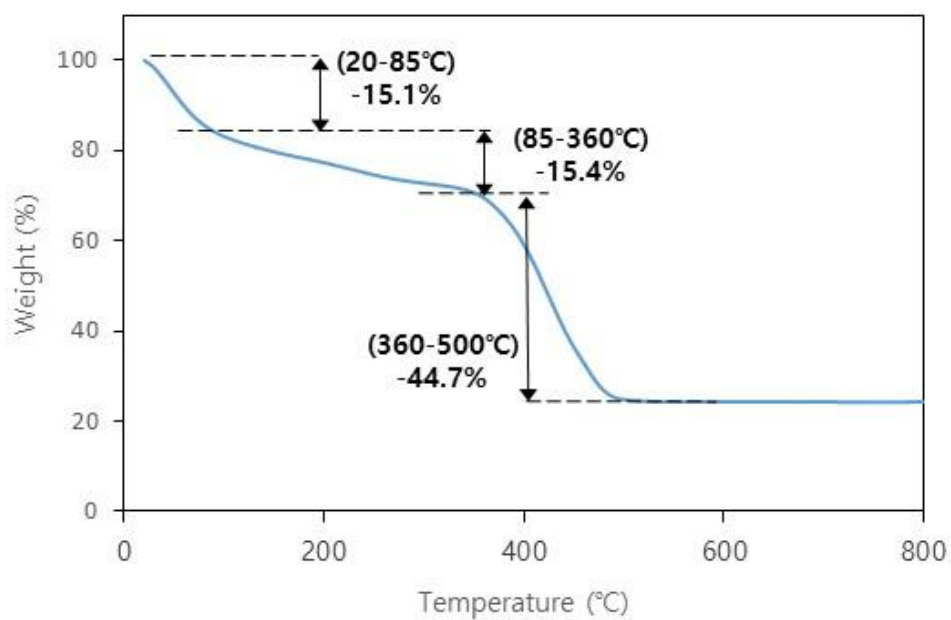


Fig. 14. TGA curve of the MIL-100(Fe)

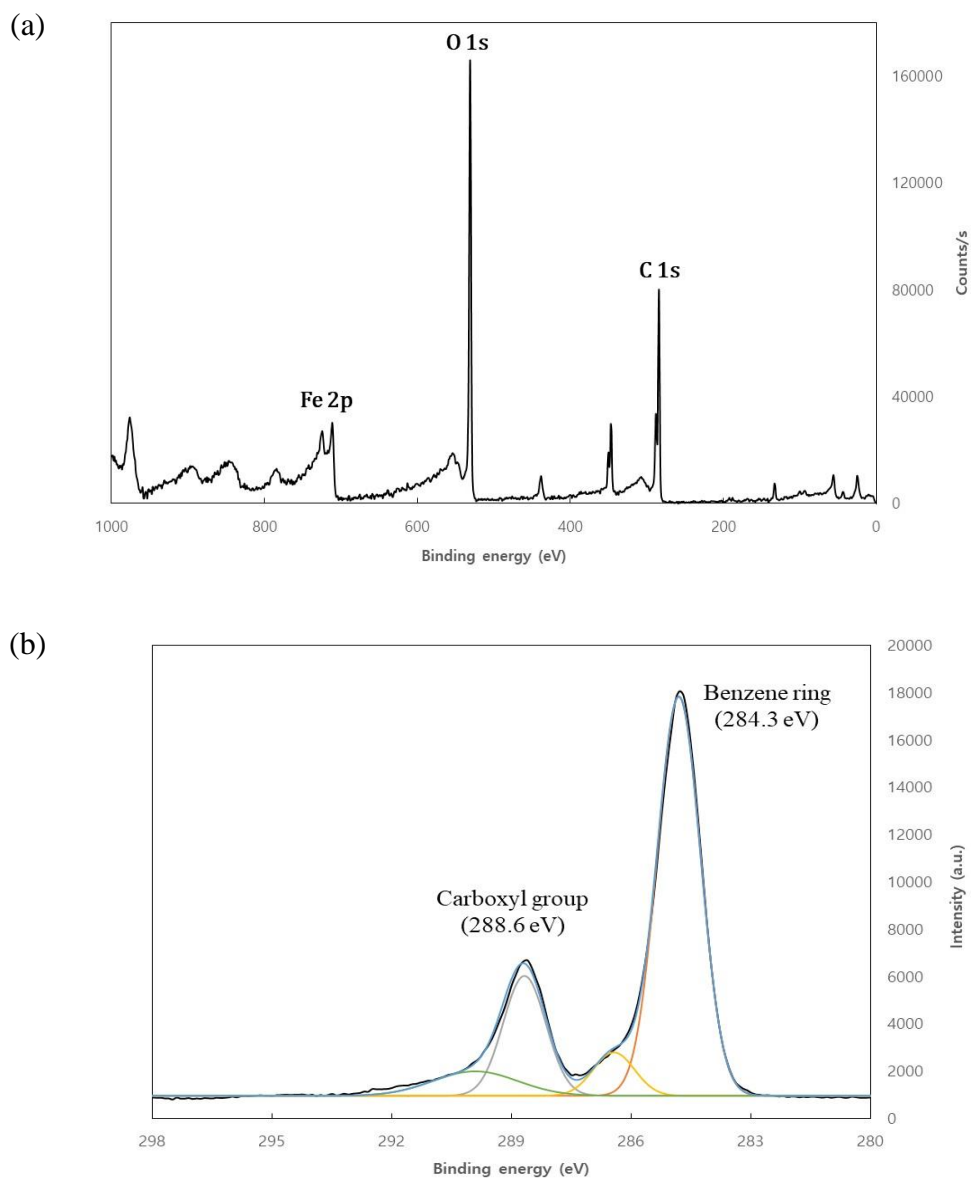


Fig. 15. XPS spectra of the MIL-100(Fe): (a) wide scan; (b) high-resolution scan of C 1s

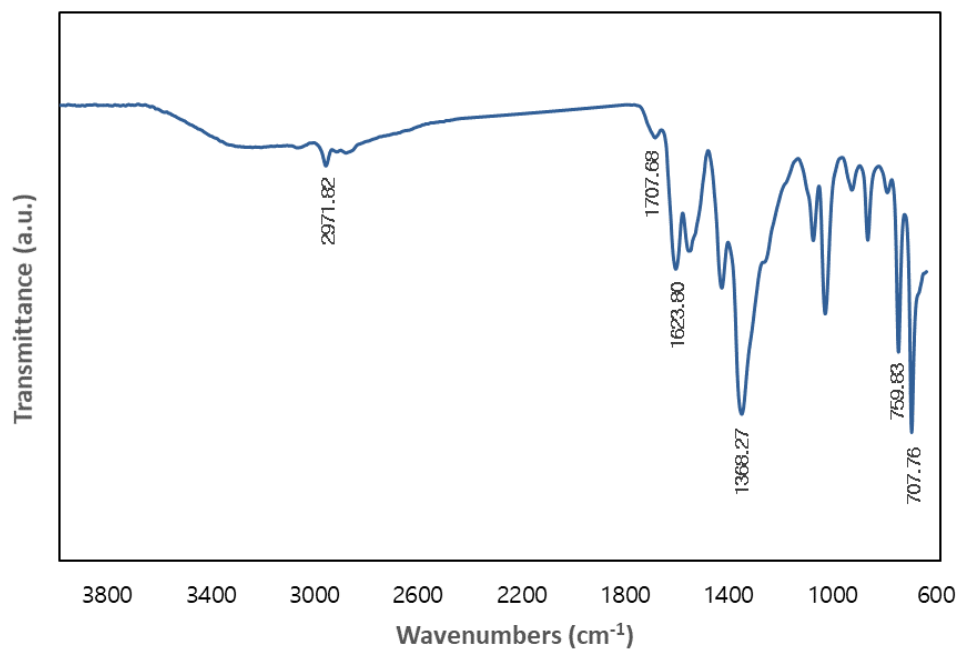


Fig. 16. FT-IR spectra of the MIL-100(Fe)

Table 10. Reduced Fe ions mass percentage (%) after the reaction (24hr)

	after the reaction (24hr)		
	Fe conc. (mg/L)	Std.	reduced Fe mass percentage (%)
DI-water	0.110	0.155	0.030
RhB	0.125	0.147	0.035
DCF	0.016	0.023	0.004

4.2. Adsorption studies for RhB

4.2.1. Single-parameter experiments for RhB removal

The isotherm data is presented in Fig. 17a and isotherm model parameters of the Langmuir, Freundlich, Redlich-Peterson isotherm models are listed in Table 11. The Langmuir model was best fitted to the isotherm data with the parameter values of $Q_m = 61.845 \text{ (mg g}^{-1}\text{)}$ and $K_L = 0.282 \text{ (L mg}^{-1}\text{)}$. The Langmuir isotherm model assumes that the adsorbate is adsorbed on the adsorbent in a monolayer and adsorption occurs at certain homogeneous sites within the adsorbent. According to the Langmuir model, when equilibrium is reached, no further adsorption occurs (Wang et al., 2020). Further, the maximum RhB adsorption capacity (Q_m) from the Langmuir model was 61.845 mg g^{-1} .

The kinetic data is presented in Fig. 17b and kinetic model parameters of the pseudo-first, pseudo-second, Elovich kinetic models are listed in Table 12. The Elovich model was best fitted to the kinetic data with the parameter values of $\alpha = 12.651$ and $\beta = 0.193$. The Elovich model assumes that the activation energy increased with reaction time and the surface of the adsorbent was heterogeneous (Wang et al., 2020). The RhB adsorption reached equilibrium in 12 hours.

The thermodynamic data analyzed with the thermodynamic models are presented in Fig. 17c. and Table 13. The entropy (ΔS°) value of $137 \text{ J K}^{-1} \text{ mol}^{-1}$ indicated that the entropy increased at the interface between solid and aqueous phases during the adsorption process. The enthalpy (ΔH°) value of 35.4 kJ mol^{-1} indicated that RhB adsorption process was endothermic, increasing adsorption capacity with increasing temperature from 20 to 40°C . The Gibb's free energy (ΔG°) values of -4.82 to $-7.56 \text{ kJ mol}^{-1}$ indicated that RhB adsorption process was spontaneous reaction. This result was in accordance with the studies Duan et al. (2016) and Navarathna et al. (2020), which had observed the endothermic reaction for RhB adsorption onto nanoscale MIL-100(Fe) and MIL-53(Fe) based hybrid adsorbent (MOF-MBC), respectively.

The adsorption data according to RhB solution pH shown in Fig. 17d. In pH range 4 to 10, high adsorption capacity is maintained around 45 mg g^{-1} . At pH 2, it shows a little lower adsorption capacity than pH 4 – 10, and adsorption hardly occurs at pH 12. The main mechanism of RhB adsorption is π - π interaction between the benzene rings of RhB and MIL-100(Fe) in most pH ranges. At $\text{pH} < 4.0$, RhB exists in the protonated form (RhB-H^+) (Liu et al., 2016). Therefore, strong electrostatic repulsion could occur

between positively charged RhB and positively charged MIL-100(Fe) ($\text{pH}_{\text{pzc}} = 4.2$). In the range of pH 4 to 10, electrostatic attraction between positively charged aminoxanthene group of RhB and negatively charged MIL-100(Fe) (Moreno-Villoslada et al, 2006; Liu et al., 2016; Mahmoodi et al., 2019). As shown in the Fig. 9f, since the crystal structure of the MIL-100(Fe) is collapsed and the RhB is unstable, adsorption hardly occurs under highly alkaline conditions (Liu et al., 2016). Schematic diagram for RhB removal mechanism by the MIL-100(Fe) is shown in Fig. 18.

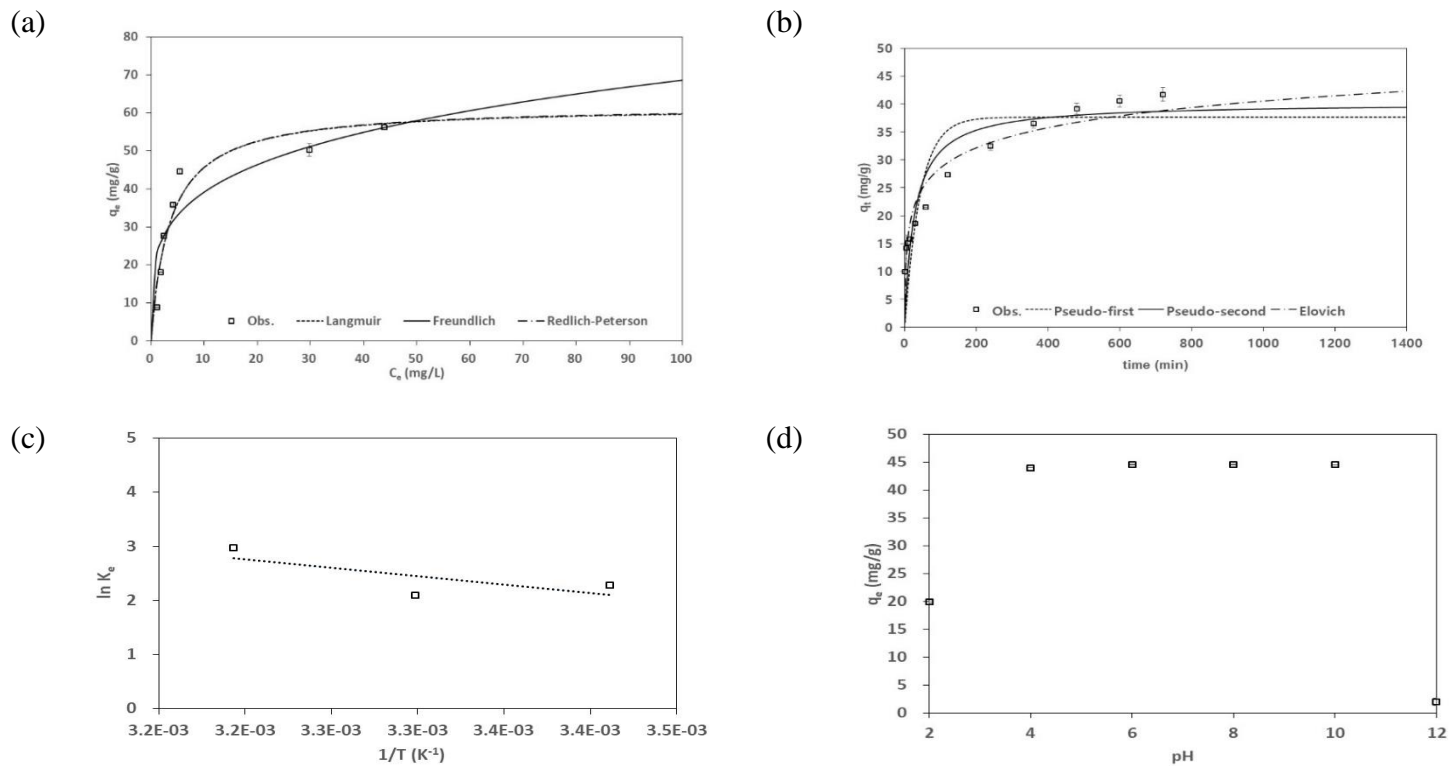


Fig. 17. Batch studies for RhB removal: (a) isotherm; (b) kinetic; (c) thermodynamic; (d) pH

Table 11. Model parameters of Langmuir, Freundlich, and Redlich-Peterson isotherm model obtained from model fitting for RhB isotherm data

Model	Langmuir isotherm model					Freundlich isotherm model					Redlich-Peterson model					
parameter	Q_m (mg/g)	K_L (L/mg)	R^2	χ^2	SAE	K_F (L/g)	1/n	R^2	χ^2	SAE	K_R (L/g)	a_R (L/mg)	g	R^2	χ^2	SAE
MIL-100(Fe)	61.845	0.282	0.922	5.336	155.668	22.384	0.243	0.804	15.213	38.070	17.492	0.284	0.999	0.922	5.351	155.676

Table 12. Model parameters of pseudo first, pseudo second, Elovich kinetic model obtained from model fitting for RhB kinetic data

Model	Pseudo first model					Pseudo second model					Elovich model				
parameter	k_1 (1/min)	q_e (mg/g)	R^2	χ^2	SAE	k_2 (g/mg/min)	q_e (mg/g)	R^2	χ^2	SAE	α	β	R^2	χ^2	SAE
MIL-100(Fe)	0.023	37.629	0.853	79.728	66.088	0.001	40.170	0.897	35.719	49.986	12.651	0.193	0.962	3.257	28.820

Table 13. Thermodynamic model parameters obtained from RhB adsorption experiments

Temp (°C)	Adsorption capacity (mg g ⁻¹)	ΔH° (kJ mol ⁻¹)	ΔS° (J K ⁻¹ mol ⁻¹)	ΔG° (kJ mol ⁻¹)
20	43.3±0.5	35.4	137	-4.82
30	43.6±0.7	35.4	137	-6.19
40	45.5±0.1	35.4	137	-7.56

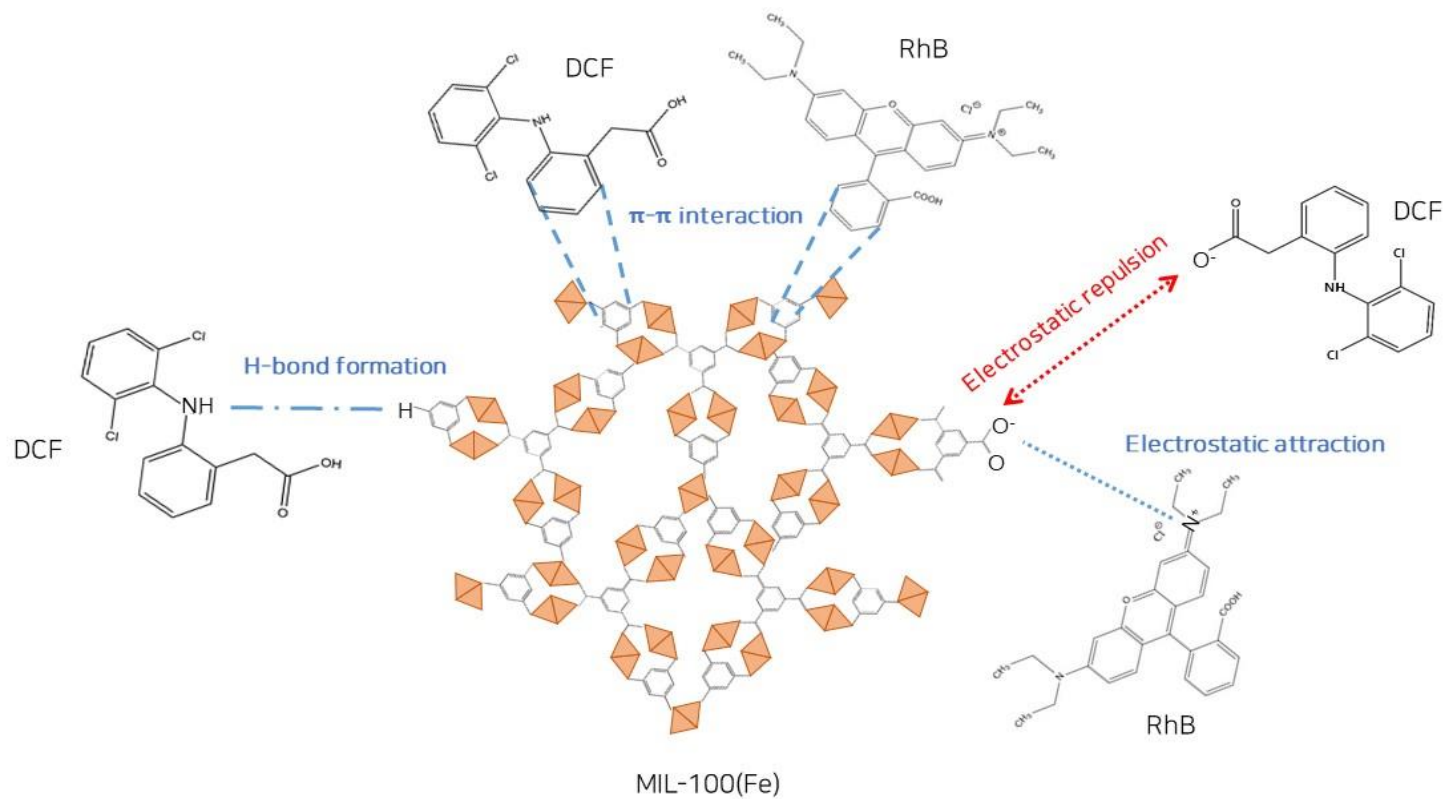


Fig. 18. Schematic diagram for RhB and DCF removal mechanism by the MIL-100(Fe)

4.2.2. Multi-parameter modeling using RSM

The CCD matrix with three input variables is presented in Table 6 along with observed removal rates and predicted values from the RSM modeling. A third order polynomial equation (cubic regression model) was developed from the experimental data in terms of coded factors using RSM follows:

$$\begin{aligned} y &= 16.07A + 15.51B - 5.91C + 0.9722AB + 2.7AC + 7.52BC - 10.14A^2 \\ &- 6.61B^2 + 1.8C^2 - 4.12ABC - 10.43A^2B - 31.49A^2C - 32.67AB^2 + 84.32 \end{aligned} \quad (20)$$

The ANOVA results of full cubic regression model from RSM are presented in Table 15. The model F -value of 57.9 indicated that the developed cubic model was significant. The lack of fit p -value 0.220 is greater than the significance level of 0.05, which means that the model is good. The coefficient of determination value (R^2) of 0.98 indicated good correlation between the observed and predicted removal rates. The adequate precision value of 22.5 also demonstrated that the developed RSM model was adequate to describe the RhB adsorption to the MIL-100(Fe) (Gadekar and Ahammed, 2019; Mahmoodi et al., 2019). The analysis showed that linear terms (A , B , C), quadratic cross-product term (BC), quadratic terms (A^2 , B^2),

and cubic cross-product terms (A^2B , A^2C , AB^2) had a large effect on the RhB adsorption to the MIL-100(Fe) due to their high F -values as well as low P -values (< 0.05). Fig. 19. illustrates the diagnostic plot between observed and predicted removal rates, indicating that the prediction of the developed cubic model was acceptable.

Fig. 20. presents the interaction effect of input variables (pH, adsorbent dose, and initial RhB concentration) on the RhB removal rate. The removal rate was influenced by the initial RhB concentration and adsorbent dose. At pH 4 and adsorbent dose of 2.0 g L^{-1} , the removal rate decreased from 94.7 to 79.7% with an increase of initial RhB concentration from 50 to 150 mg L^{-1} . As the adsorbent dose increased from 1.0 to 3.0 g L^{-1} at pH 4 and initial RhB concentration of 100 mg L^{-1} , the removal rate increased from 54.1 to 93.4% (Fig. 20a, 20b). The removal rate was also affected by solution pH. At the adsorbent dose of 2.0 g L^{-1} and initial RhB concentration of 100 mg L^{-1} , the removal rate increased from 44.8 to 88.4% with a change of pH from 2 to 6 (Fig. 20c, 20d). As presented in Table 15, the regressor variable of 'A' (pH) had a larger coefficient value (16.1) than 'B' (adsorbent dose) and 'C' (initial RhB concentration), indicating that pH had a higher impact on the RhB removal rate than other input variables.

Table 14. Observed removal rates and predicted values from RSM modeling for RhB adsorption

Ex.	Input variable			RhB removal rate (%)	
	Initial pH	MIL-100(Fe) dosage (g/L)	Initial RhB concentration (mg/L)	Observed	Predicted from RSM
1	2.0	2.0	100	48.4±0.49	47.7
2	4.0	1.0	100	54.8±2.77	54.1
3	4.0	2.0	50	95.3±0.57	94.6
4	4.0	2.0	150	80.4±1.94	79.7
5	4.0	3.0	100	94.0±1.07	93.3
6	6.0	2.0	100	89.1±0.92	88.4
7	3.0	1.5	75	85.8±0.81	86.4
8	3.0	1.5	125	52.2±2.49	52.8
9	3.0	2.5	75	91.3±0.57	91.9
10	3.0	2.5	125	73.8±1.44	74.4
11	5.0	1.5	75	84.6±2.33	85.2
12	5.0	1.5	125	59.4±0.97	60.0
13	5.0	2.5	75	95.8±0.15	96.4
14	5.0	2.5	125	78.5±3.26	79.1
15	4.0	2.0	100	85.6±5.67	84.3

Table 15. ANOVA results of full cubic regression model from RSM

Source	Coefficient estimate	Sum of squares	Degrees of freedom	Mean square	F-value	P-value	
Model		7556.85	13	581.3	57.91	< 0.0001	significant
Intercept	84.32						
A	16.07	1653.52	1	1653.52	164.73	< 0.0001	
B	15.51	1539.11	1	1539.11	153.33	< 0.0001	
C	-5.91	223.62	1	223.62	22.28	0.0002	
AB	0.9722	2.42	1	2.42	0.241	0.6301	
AC	2.70	18.64	1	18.64	1.86	0.1918	
BC	7.52	144.94	1	144.94	14.44	0.0016	
A ²	-10.14	364.15	1	364.15	36.28	< 0.0001	
B ²	-6.61	154.93	1	154.93	15.44	0.0012	
C ²	1.80	11.52	1	11.52	1.15	0.3	
ABC	-4.12	17.41	1	17.41	1.73	0.2063	

A ² B	-10.43	55.66	1	55.66	5.55	0.0316	
A ² C	-31.49	507.64	1	507.64	50.57	< 0.0001	
AB ²	-32.67	546.37	1	546.37	54.43	< 0.0001	
AC ²	aliased	0	0				
B ² C	aliased	0	0				
BC ²	aliased	0	0				
A ³	aliased	0	0				
B ³	aliased	0	0				
C ³	aliased	0	0				
Residual		160.6	16	10.04			
Lack of fit		15.81	1	15.81	1.64	0.2201	not significant
Pure error		144.8	15	9.65			

R² = 0.98; Adjusted R² = 0.96; Predicted R² = 0.93; Adequate precision = 22.50

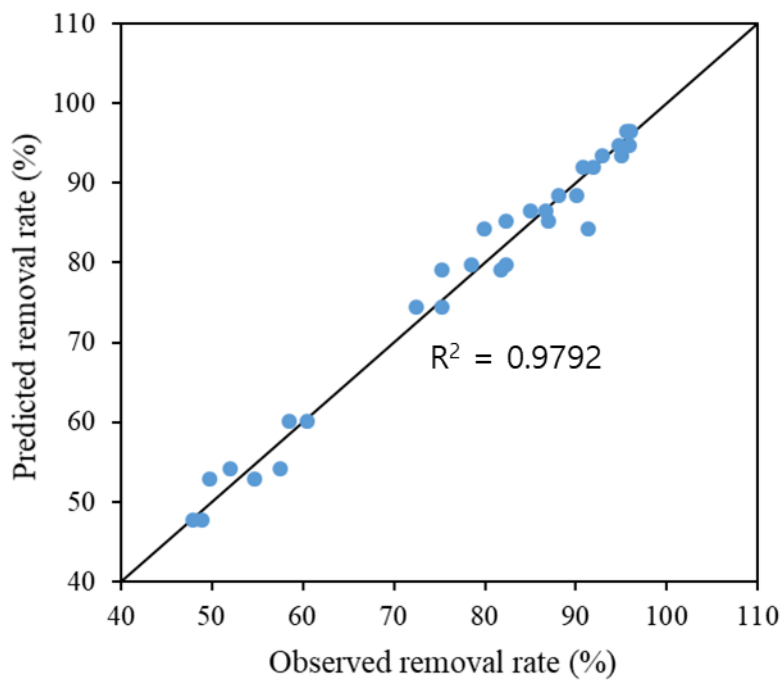


Figure 19. Diagnostic plot between observed and predicted removal rates from the RSM model

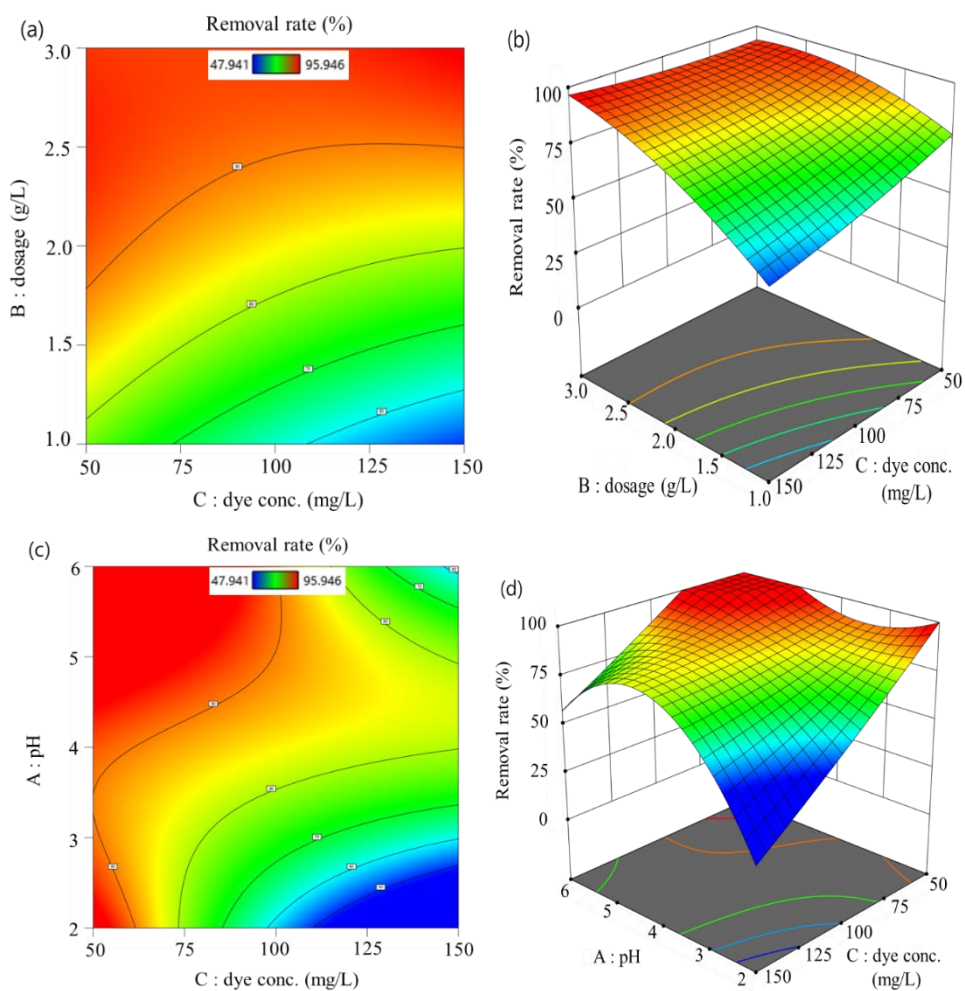


Figure 20. Interaction effect of input variables on the RhB removal rate: (a) 2-D plot (at pH 4) between initial RhB concentration and adsorbent dose; (b) 3-D plot (at pH 4) between initial RhB concentration and adsorbent dose; (c) 2-D plot (at adsorbent dose of 2.0 g/L) between initial RhB concentration and pH; and (d) 3-D plot (at adsorbent dose of 2.0 g/L) between initial RhB concentration and pH

4.2.3. Multi-parameter modeling using ANN

The three input variables set for ANN modeling for the RhB removal experiment are pH (A), adsorbent dose (B), and RhB initial concentration (C) normalized from -1 to +1, and the output variable is the RhB removal rate (%). The structure of the ANN model is shown in Fig. 21a, which is determined by the number of hidden layers and the number of neurons (Sharafi et al., 2019). In order to find the optimal ANN structure, the number of neurons in the hidden layer was adjusted from 6 to 10 and the topology with the minimum MSE value and R value close to 1. Furthermore, by increasing the number of hidden layers to 2, the number of neurons was adjusted from 6 to 10 (Table 16.).

The topology 3:6:1 was selected with the smallest MSE value (0.611), which means 3 input variables, 1 hidden layer, 6 neurons, and 1 output value. The values of weights (w) and biases (b) for each layer and neuron in equation (21) are tabulated in Table 17.

$$y = \sum_{n=1}^8 \left\{ \left(\frac{2}{1 + \exp \left[-2 \left((A \times w_{A,n} + B \times w_{B,n} + C \times w_{C,n}) + b_n \right) \right]} - 1 \right) \times w_{O,n} \right\} + b_o \quad (21)$$

where, A, B, C are the input variables which is the pH, adsorbent dose, initial RhB concentration, respectively. $w_{A,n}$, $w_{B,n}$ and $w_{C,n}$ are the weight of input A, B and C in hidden layer n^{th} neuron, respectively. $w_{O,n}$ is the weight in output layer, b_n is the bias in hidden layer n^{th} neuron, and b_O is the bias in output layer.

The value of observed removal rates and predicted values from ANN modeling are shown in Table 18. and linear fit for experimental and predicted removal rate are shown in Fig. 22.

In other to further examine the predictability of the ANN model for the RhB removal, additional adsorption experiments were conducted in the experimental conditions, which were not previously included in Table 6. Four experimental conditions were randomly selected in the range of the input variables applied for the CCD matrix using the random number generator function (RAND) in Excel software (Microsoft, Redmond, WA, USA). Additional experiments were performed in duplicate for each condition (N = 8). The observed and predicted from ANN model values are shown in Table 19, and diagnostic plots between observed and predicted removal rates are shown in Fig. 23, which is demonstrated the ANN model shows a prediction accuracy of $R^2 = 0.821$.

Furthermore, in order to determine the most influential input variable on the RhB removal rate, the impacts of three input variables were compared based on the following formulas (Samui et al., 2018):

$$I_i(\%) = \frac{\sum_{n=1}^8 \left[\frac{|w_{i,n}| \times |w_{o,n}|}{\sum_{i=1}^3 (|w_{i,n}| \times |w_{o,n}|)} \right]}{\max \left\{ \sum_{n=1}^8 \left[\frac{|w_{A,n}| \times |w_{o,n}|}{\sum_{i=1}^3 (|w_{i,n}| \times |w_{o,n}|)} \right], \sum_{n=1}^8 \left[\frac{|w_{B,n}| \times |w_{o,n}|}{\sum_{i=1}^3 (|w_{i,n}| \times |w_{o,n}|)} \right], \sum_{n=1}^8 \left[\frac{|w_{C,n}| \times |w_{o,n}|}{\sum_{i=1}^3 (|w_{i,n}| \times |w_{o,n}|)} \right] \right\}} \times 100 \quad (22)$$

where, I_i is the relative importance of each input variable (%), i is the input variable (A : $i = 1$, B : $i = 2$, C : $i = 3$), n is the number of neuron, $w_{i,n}$ is the weight of input variable 'i' in hidden layer n^{th} neuron and $w_{o,n}$ is the weight in output layer n^{th} neuron. The relative importance of the input variable was in the decreasing order of pH (100%) > initial RB concentration (60.7%) > adsorbent dosage (46.7%) (Fig. 24.). The analyses showed that pH was the most important input variable affecting the RhB removal rate.

Based on the ANN model, the optimal condition for the RhB adsorption was determined using the MATLAB nntool. Input variable conditions with the RhB removal rate exceeding 99.8% are shown in Table 20, and the condition showing the optimal removal rate (99.953%) was pH 5.3, adsorbent dose 2.0 g L^{-1} , and initial RhB concentration 73 mg L^{-1} .

Table 16. Comparison of network topologies with various hidden layers and neurons for RhB removal

Topology	MSE	R			
		Training	Validating	Testing	All
3:6:1	3.456	0.993	0.991	0.966	0.984
3:7:1	27.964	0.993	0.961	0.974	0.887
3:8:1	0.611	0.975	0.998	0.954	0.975
3:9:1	9.194	0.988	0.988	0.211	0.961
3:10:1	437.366	0.987	0.559	0.996	0.850
3:6:6:1	8.868	0.990	0.979	0.977	0.987
3:6:7:1	119.692	0.978	0.735	0.437	0.880
3:6:8:1	84.410	0.989	0.845	-0.478	0.741
3:6:9:1	32.813	0.998	0.973	0.424	0.966
3:6:10:1	27.512	0.984	0.661	0.069	0.783
3:7:6:1	224.319	0.988	0.880	0.876	0.897
3:7:7:1	16.05	0.991	0.981	0.966	0.984
3:7:8:1	33.407	0.841	0.652	0.845	0.801
3:7:9:1	192.907	0.800	0.487	0.317	0.750
3:7:10:1	93.817	0.994	0.836	0.867	0.947
3:8:6:1	52.587	0.921	0.886	0.965	0.904
3:8:7:1	86.346	0.995	0.905	0.981	0.966
3:8:8:1	4.035	0.994	0.990	0.847	0.902
3:8:9:1	19.936	0.902	0.678	0.989	0.918
3:8:10:1	9.324	0.992	0.997	0.971	0.966
3:9:6:1	5.867	0.985	0.999	0.991	0.988
3:9:7:1	50.389	0.997	0.939	0.943	0.974
3:9:8:1	631.141	0.592	-0.041	0.985	0.527
3:9:9:1	16.821	0.996	0.985	0.957	0.983
3:9:10:1	86.302	0.912	0.895	0.809	0.879
3:10:6:1	125.318	0.706	-0.925	-0.064	0.575
3:10:7:1	92.761	0.996	0.868	0.847	0.951
3:10:8:1	22.430	0.992	0.974	0.972	0.979
3:10:9:1	86.591	0.921	0.972	0.466	0.838
3:10:10:1	4.722	0.895	0.950	0.971	0.915

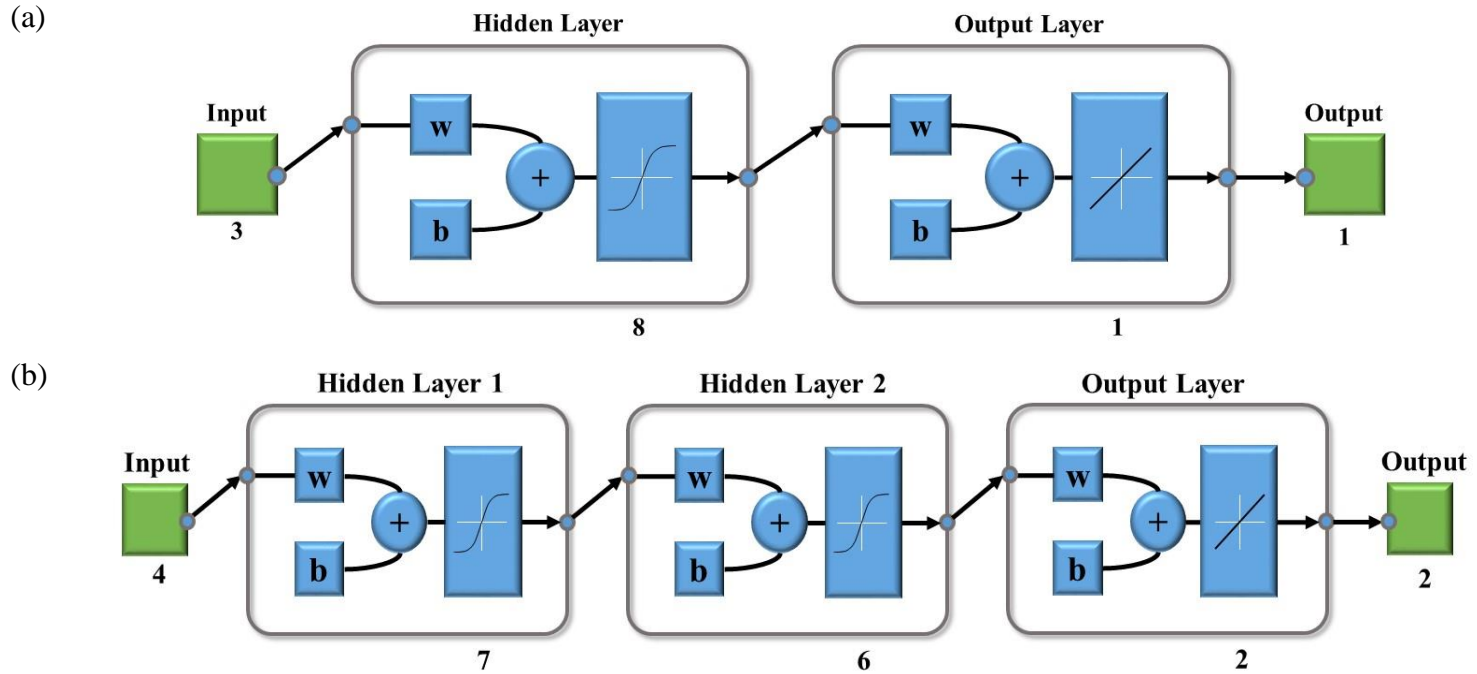


Fig. 21. Schematic diagram of artificial neural network (ANN) structure: (a) for the RhB adsorption; and (b) DCF adsorption

Table 17. Values of weights and biases for each layer and neuron in equation (17)

Neuron (n =)	Hidden layer				Output layer	
	$w_{A,n}$	$w_{B,n}$	$w_{C,n}$	b_n	$w_{O,n}$	b_o
1	2.3461	0.8756	-1.7888	-2.5596	0.7407	-0.1591
2	-1.1418	-2.1424	-0.9696	2.3829	0.4764	
3	2.7816	0.7037	-0.6895	-1.3420	0.6192	
4	-3.0286	0.8979	0.7515	0.5915	1.0438	
5	-1.6036	-1.8158	-1.8032	-1.5282	-0.2951	
6	-2.5224	-0.6362	0.7804	-1.3894	-0.9984	
7	0.8832	1.4561	2.2611	2.0171	-0.7749	
8	1.6254	0.4477	-2.1502	2.9543	0.5799	

$w_{A,n}$ = weight of input A in hidden layer n^{th} neuron, $w_{B,n}$ = weight of input B in hidden layer n^{th} neuron, $w_{C,n}$ = weight of input C in hidden layer n^{th} neuron, b_n = bias in hidden layer n^{th} neuron, $w_{O,n}$ = weight in output layer n^{th} neuron, b_o = bias in output layer.

Table 18. Observed removal rates and predicted values from ANN modeling for RhB adsorption (Topology 3:6:1)

Ex.	Input variable			RhB removal rate (%)	
	Initial pH	MIL-100(Fe) dosage (g/L)	Initial RhB concentration (mg/L)	Observed	Predicted from ANN
1	2.0	2.0	100	48.4±0.49	48.4
2	4.0	1.0	100	54.8±2.77	57.6
3	4.0	2.0	50	95.3±0.57	95.3
4	4.0	2.0	150	80.4±1.94	80.4
5	4.0	3.0	100	94.0±1.07	86.6
6	6.0	2.0	100	89.1±0.92	89.1
7	3.0	1.5	75	85.8±0.81	86.6
8	3.0	1.5	125	52.2±2.49	52.2
9	3.0	2.5	75	91.3±0.57	90.8
10	3.0	2.5	125	73.8±1.44	73.8
11	5.0	1.5	75	84.6±2.33	91.1
12	5.0	1.5	125	59.4±0.97	60.4
13	5.0	2.5	75	95.8±0.15	96.0
14	5.0	2.5	125	78.5±3.26	75.2
15	4.0	2.0	100	85.6±5.67	85.7

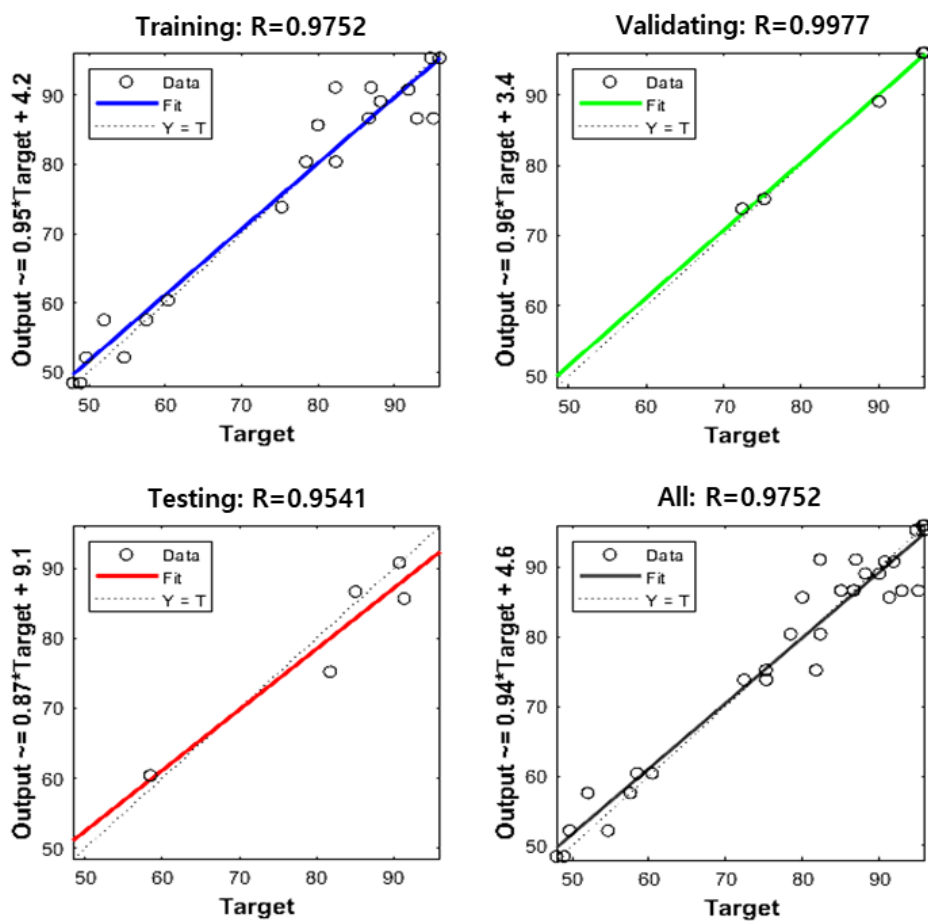


Fig. 22. Linear fit for experimental and predicted RhB removal rate

Table 19. Additional experimental conditions along with observed and predicted from the ANN model values for RhB removal rates

Exp.	Input variable			Removal rate (%)	
	pH (A)	Adsorbent dose (B)	Initial RhB conc. (C)	Observed	Predicted-ANN
A1	3.1	1.5	107	60.629	59.130
A2	3.0	2.0	60	87.851	85.587
A3	4.1	2.7	72	95.072	95.687
A4	4.2	2.5	121	75.049	86.882
A5	3.1	1.5	107	68.751	59.130
A6	3.0	2.0	60	88.661	85.587
A7	4.1	2.7	72	96.184	95.687
A8	4.2	2.5	121	82.544	86.882

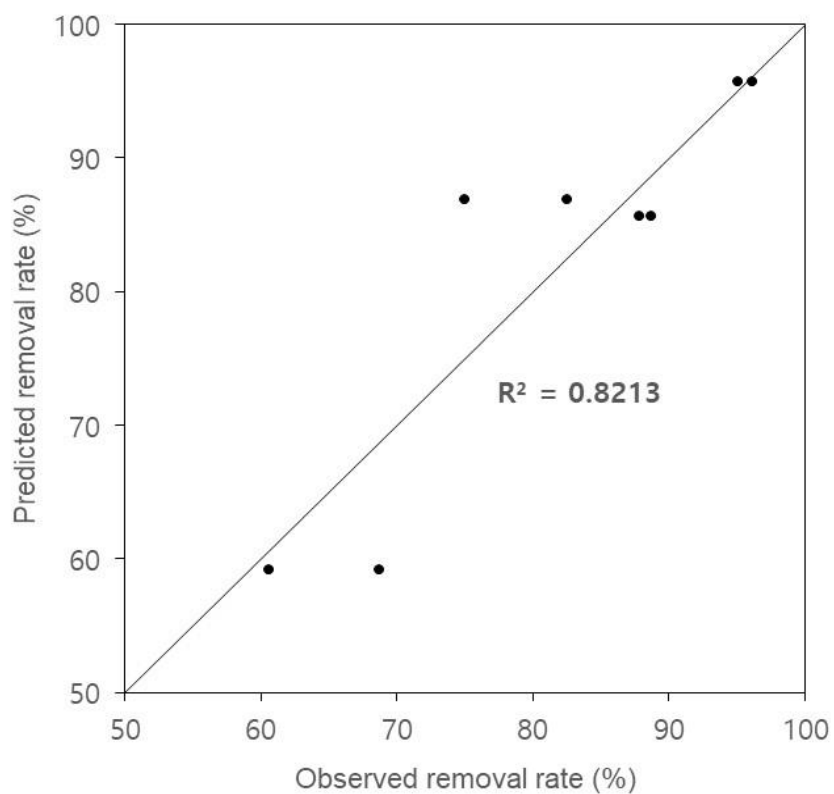


Fig. 23. Diagnostic plot between observed and predicted values from additional experiments for RhB removal rate

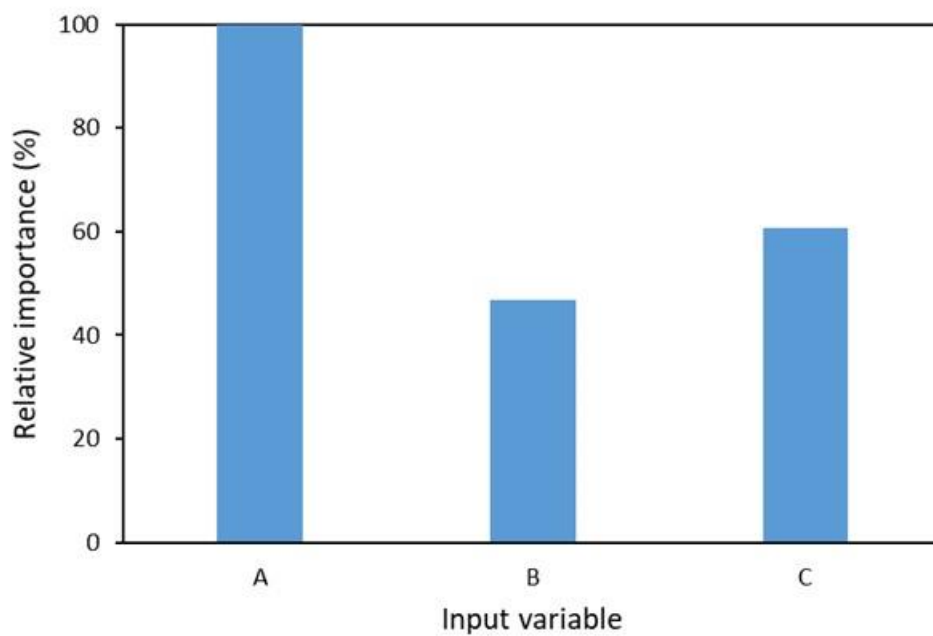


Fig. 24. Relative importance of three input variables on the RhB removal rate

Table 20. Optimum condition for RhB removal by the MIL-100(Fe) from ANN model

pH (A)	Input variable		Removal rate (%)
	Adsorbent dose (B)	Initial RhB conc. (C)	
5.3	2.0	73	99.953
5.2	2.5	71	99.898
5.9	2.2	90	99.887
5.5	1.7	79	99.823
5.5	2.0	81	99.817

4.3. Adsorption studies for DCF

4.3.1. Single-parameter experiments for DCF removal

In a similar way to fitting the RhB adsorption experiments, the DCF isotherm data is presented in Fig. 25a and isotherm model parameters of the Langmuir, Freundlich, Redlich-Peterson isotherm models are listed in Table 21. The Langmuir and Redlich-Peterson model were best fitted to the isotherm data with the parameter values of $Q_m = 414.581 \text{ (mg g}^{-1}\text{)}$, $K_L = 0.022 \text{ (L mg}^{-1}\text{)}$ and $K_R = 8.949 \text{ (L g}^{-1}\text{)}$, $a_R = 0.022 \text{ (L mg}^{-1}\text{)}$, $g = 0.999$, respectively. The Redlich-Peterson isotherm model is an empirical model that combines Langmuir and Freundlich models applied to homogeneous or heterogeneous adsorption studies. This model approaches the Langmuir model when $g = 1$ (Wang et al., 2020). Further, the maximum DCF adsorption capacity (Q_m) from the Langmuir model was $414.581 \text{ mg g}^{-1}$.

The kinetic data is presented in Fig. 25b and kinetic model parameters of the pseudo-first, pseudo-second, Elovich kinetic models are listed in Table 22. The Pseudo-second model was best fitted to the kinetic data with the parameter values of $k_2 = 0.000056 \text{ (g mg}^{-1} \text{ min}^{-1}\text{)}$ and $q_e = 227.708 \text{ (mg g}^{-1}\text{)}$. In the pseudo second-order model, the adsorption rate and $(q_e - q_t)$ are proportional to the second order. Furthermore, when initial DCF solution

concentration (C_0) was low, the Langmuir kinetics model could be simplified to the Pseudo-second order model (Wang et al., 2020). The DCF adsorption reached equilibrium in 12 hours.

The thermodynamic data analyzed with the thermodynamic models are presented in Fig. 25c. and Table 23. The entropy (ΔS°) value of $14.2 \text{ J K}^{-1} \text{ mol}^{-1}$ indicated that the entropy increased at the interface between solid and aqueous phases during the adsorption process. The enthalpy (ΔH°) value of 3.87 kJ mol^{-1} indicated that DCF adsorption process was endothermic, increasing adsorption capacity with increasing temperature from 10 to 50°C . The Gibb's free energy (ΔG°) values of -0.148 to $-0.716 \text{ kJ mol}^{-1}$ indicated that DCF adsorption process was spontaneous reaction. This result was in accordance with the studies Zheng et al. (2018) and Zhuang et al. (2019), which had observed the endothermic reaction for DCF adsorption onto $\text{Fe}_3\text{O}_4@\text{MOF-100}(\text{Fe})$ magnetic composites and UiO-66-type MOFs, respectively. Contrarily, Luo et al. (2018) and Liu et al. (2019) were reported the exothermic reaction for DCF adsorption onto Cu-based MOFs.

The adsorption data according to DCF solution pH shown in Fig. 25d. In pH range 5 to 10, the adsorption capacity gradually decreased from 281.2 to 131.0 mg g^{-1} . At pH 12, the removal capacity became negligible. The π - π

interaction between the benzene rings of DCF and MIL-100(Fe) and H-bonding could play important roles in the DCF adsorption process. In the range of pH 5 to 10, it shows electrostatic repulsion due to the negative charges of DCF and MIL-100(Fe) surface. As the pH increases, the magnitude of the negative charge increases and the electrostatic repulsive force increases. Further, DCF adsorption onto the MIL-100(Fe) hardly occurs at pH 12 due to the instability of crystal structure of the MIL-100(Fe). Schematic diagram for DCF removal mechanism by the MIL-100(Fe) is shown in Fig. 18.

Unlike RhB removal, where the difference before and after adsorption can be visually confirmed, DCF is not visible before and after adsorption. Therefore, XPS and FTIR before and after adsorption were additionally analyzed to confirm whether DCF was adsorbed to MIL-100(Fe) well. The wide scan XPS spectra of the MIL-100(Fe) before and after adsorption are shown in Fig. 26. In Fig. 26b, there are new peaks at 399.6 eV, 200.2 eV and 201.8 eV, corresponding to N 1s, Cl 2p_{3/2} and Cl 2p_{1/2} from the DCF, respectively. Furthermore, in the FTIR spectra of the MIL-100(Fe) before and after adsorption (Fig. 27.), two additional peaks appeared at 762 cm⁻¹ and 3060 cm⁻¹, corresponding to C-Cl stretching and C-H stretching from the DCF, respectively. Through the XPS and FTIR spectrum, we could confirm

adsorption of DCF onto the surface of the MIL-100(Fe).

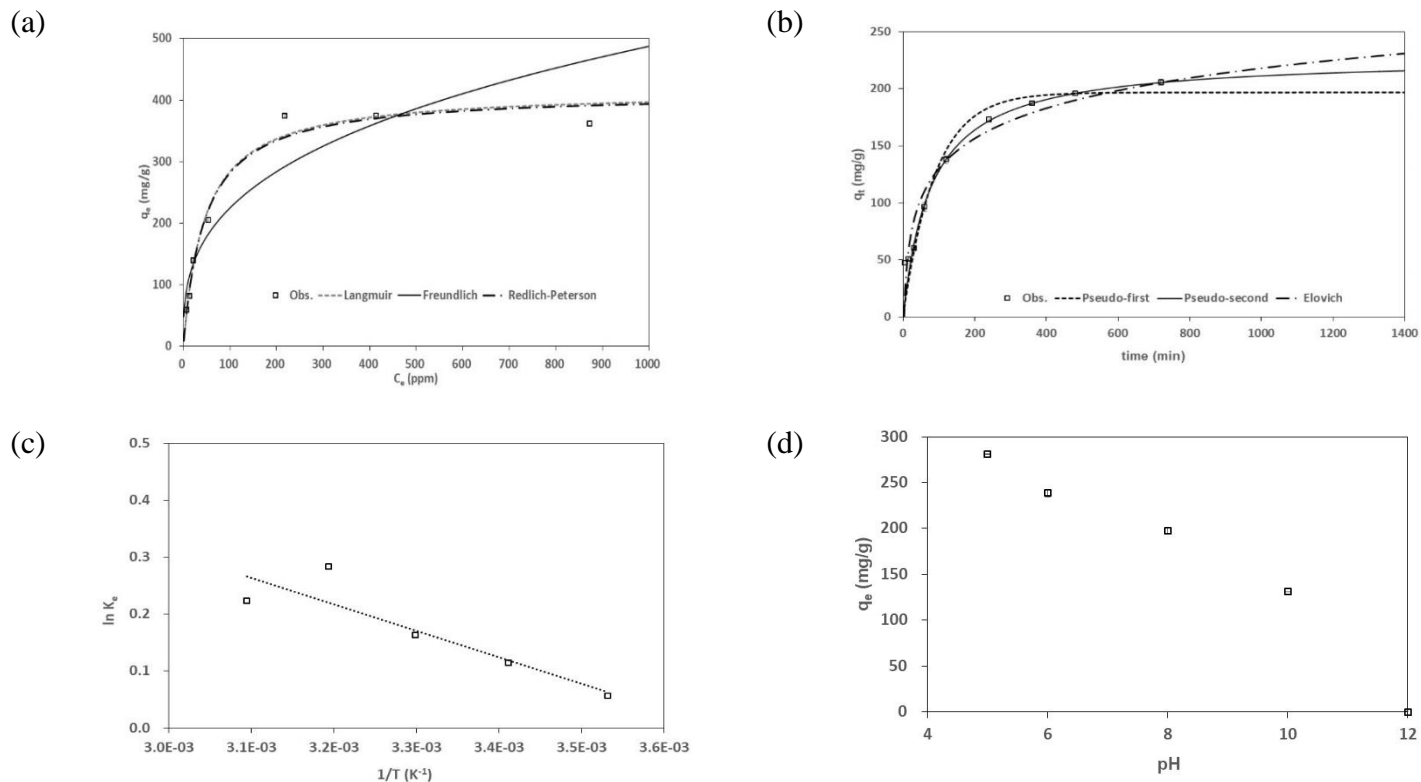


Fig. 25. Batch studies for DCF removal: (a) isotherm; (b) kinetic; (c) thermodynamic; (d) pH

Table 21. Model parameters of Langmuir, Freundlich, and Redlich-Peterson isotherm model obtained from model fitting for DCF isotherm data

Model	Langmuir isotherm model					Freundlich isotherm model					Redlich-Peterson model					
parameter	Q_m (mg/g)	K_L (L/mg)	R^2	χ^2	SAE	K_F (L/g)	1/n	R^2	χ^2	SAE	K_R (L/g)	a_R (L/mg)	g	R^2	χ^2	SAE
MIL-100(Fe)	414.581	0.022	0.979	8.662	1048.726	47.587	0.337	0.839	71.659	294.720	8.949	0.022	0.999	0.979	8.678	1049.832

Table 22. Model parameters of pseudo first, pseudo second, Elovich kinetic model obtained from model fitting for DCF kinetic data

Model	Pseudo first model					Pseudo second model					Elovich model				
parameter	k_1 (1/min)	q_e (mg/g)	R^2	χ^2	SAE	k_2 (g/mg/min)	q_e (mg/g)	R^2	χ^2	SAE	α	β	R^2	χ^2	SAE
MIL-100(Fe)	0.011	196.771	0.968	141.642	113.287	0.000056	227.705	0.984	88.075	54.885	11.470	0.026	0.948	76.794	116.652

Table 23. Thermodynamic model parameters obtained from DCF adsorption experiments

Temperature (K)	ΔG° (kJ/mol)	ΔS° (J/ K·mol)	ΔH° (kJ/mol)
283.15	-0.148	14.2	3.87
293.15	-0.290	14.2	3.87
303.15	-0.432	14.2	3.87
313.15	-0.574	14.2	3.87
323.15	-0.716	14.2	3.87

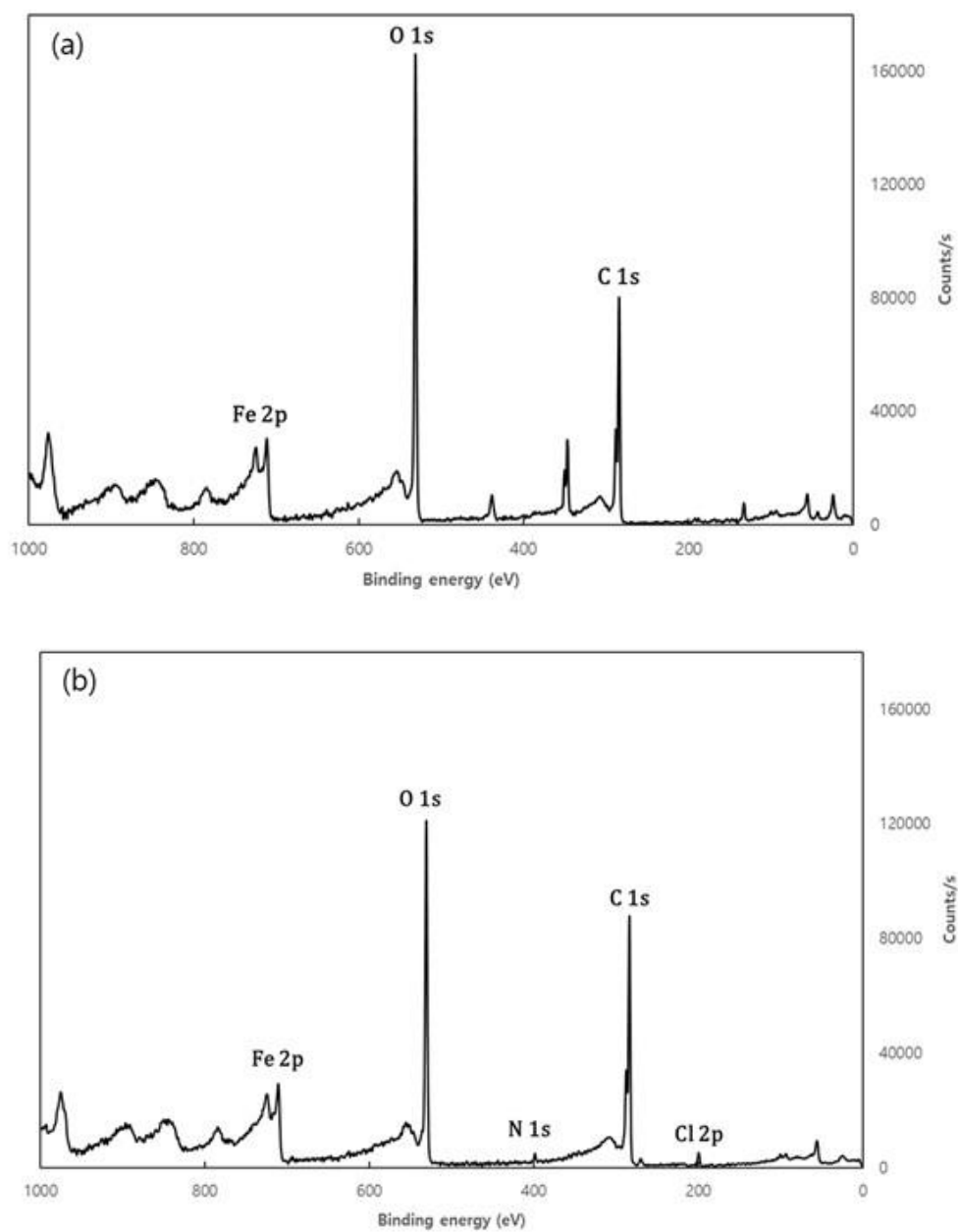


Fig. 26. The wide scan XPS spectra of the MIL-100(Fe): (a) before and; (b) after adsorption

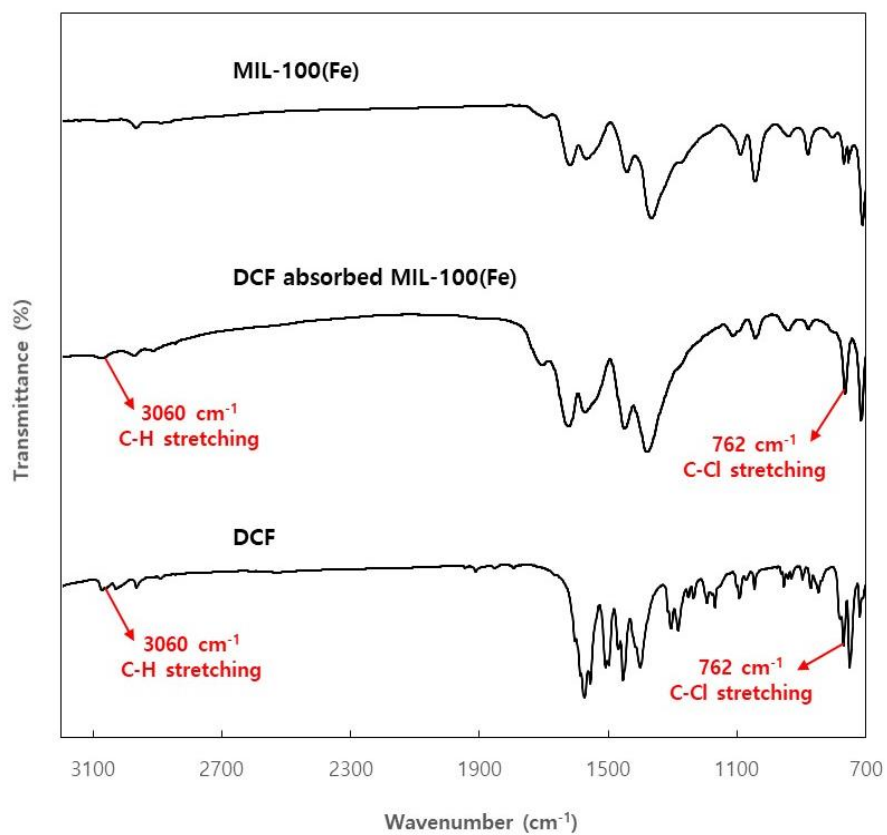


Fig. 27. The FTIR spectra of the MIL-100(Fe) before and after adsorption

4.3.2. Multi-parameter modeling using ANN

The four input variables set for ANN modeling for the DCF removal experiment are initial pH (A), adsorbent dose (B), DCF initial concentration (C), and temperature (D) normalized from -1 to +1, and the output variables are the DCF removal rate (%) and final pH. The structure of the ANN model is shown in Fig. 21b. In order to find the optimal ANN structure, the number of neurons in the hidden layer was adjusted from 6 to 10 and the topology with the minimum MSE value and R value closed to 1. Furthermore, by increasing the number of hidden layers to 2, the number of neurons in each layer was adjusted from 6 to 10 (Table 24.).

The topology 4:7:6:2 was selected with the lowest MSE value (0.119), which means 4 input variables, 2 hidden layers, 7 neurons in the first-hidden layer, 6 neurons in the second-hidden layer, and 2 output value. The values of weights (w) and biases (b) for each layer and neuron in equation (23) are tabulated in Table 25.

$$\begin{bmatrix} h_{1,1} \\ \vdots \\ h_{1,7} \end{bmatrix} = \text{tansig} \left(\begin{bmatrix} \vec{w}_{1,1} \\ \vdots \\ \vec{w}_{1,7} \end{bmatrix} \times \begin{bmatrix} x_1 \\ x_2 \\ x_3 \\ x_4 \end{bmatrix} + \begin{bmatrix} b_{1,1} \\ \vdots \\ b_{1,7} \end{bmatrix} \right) \quad (23)$$

$$\begin{bmatrix} h_{2,1} \\ \vdots \\ h_{2,6} \end{bmatrix} = \text{tansig} \left(\begin{bmatrix} \vec{w}_{2,1} \\ \vdots \\ \vec{w}_{2,6} \end{bmatrix} \times \begin{bmatrix} h_{1,1} \\ \vdots \\ h_{1,7} \end{bmatrix} + \begin{bmatrix} b_{2,1} \\ \vdots \\ b_{2,6} \end{bmatrix} \right)$$

$$\begin{bmatrix} f_1 \\ f_2 \end{bmatrix} = \text{purelin} \left(\begin{bmatrix} \vec{w}_{o,1} \\ \vec{w}_{o,2} \end{bmatrix} \times \begin{bmatrix} h_{2,1} \\ \vdots \\ h_{2,6} \end{bmatrix} + \begin{bmatrix} b_{o,1} \\ b_{o,2} \end{bmatrix} \right)$$

where, $w_{1,n}$, $w_{2,n}$ and $w_{o,n}$ are the weight of each input variable in first-hidden layer n^{th} neuron, second-hidden layer n^{th} neuron and output layer n^{th} neuron, respectively. $b_{1,n}$, $b_{2,n}$ and $b_{o,n}$ is the bias in first-hidden layer n^{th} neuron, second-hidden layer n^{th} neuron and output layer n^{th} neuron, respectively.

The value of observed removal rates and predicted values from ANN modeling are shown in Table 26. and linear fit for experimental and predicted removal rate are shown in Fig. 28.

In other to further examine the predictability of the ANN model for the DCF removal (removal rate and final pH), additional adsorption experiments were conducted in the experimental conditions, which were not previously included in Table 9. Three experimental conditions were randomly selected in the range of the input variables applied for the CCD matrix using the random number generator function (RAND) in Excel software (Microsoft, Redmond,

WA, USA). Additional experiments were performed in duplicate for each condition ($N = 6$). The observed and predicted from ANN model values are shown in Table 27, and diagnostic plots between observed and predicted removal rates and final pH are shown in Fig. 29, which are demonstrated the ANN model shows a prediction accuracy of $R^2 = 0.967$ and $R^2 = 0.903$, respectively.

Furthermore, in order to determine the most influential input variable on the DCF removal rate, the impacts of four input variables were compared based on the formula (24) (Samui et al., 2018). The relative importance of the input variable was in the order of temperature (100%) > adsorbent dosage (90.2%) > initial pH (71.8%) > initial DCF concentration (59.3%) (Fig. 30.). The analyses showed that temperature was the most important input variable affecting the DCF removal rate.

Based on the ANN model, the optimal condition for the DCF adsorption was determined using the MATLAB nntool. Input variable conditions with the DCF removal rate exceeding 99.5% are shown in Table 28, and the condition showing the optimal removal rate (99.9%) was initial pH 6.1, adsorbent dose 0.5 g L^{-1} , initial DCF concentration 63 mg L^{-1} , and temperature $22 \text{ }^{\circ}\text{C}$.

$$\begin{aligned}
& I_i(\%) \\
& = \frac{\sum_{n=1}^7 \left[\frac{|\vec{w}_{(1)i,n}| \times |\vec{w}_{(2)n}| \times |\vec{w}_{(O)n}|}{(|\vec{w}_{(1)}| \times |\vec{w}_{(2)n}| \times |\vec{w}_{(O)n}|)} \right]}{\max \left\{ \sum_{n=1}^7 \left[\frac{|\vec{w}_{(1)A,n}| \times |\vec{w}_{(2)n}| \times |\vec{w}_{(O)n}|}{(|\vec{w}_{(1)}| \times |\vec{w}_{(2)n}| \times |\vec{w}_{(O)n}|)} \right], \sum_{n=1}^7 \left[\frac{|\vec{w}_{(1)B,n}| \times |\vec{w}_{(2)n}| \times |\vec{w}_{(O)n}|}{(|\vec{w}_{(1)}| \times |\vec{w}_{(2)n}| \times |\vec{w}_{(O)n}|)} \right], \sum_{n=1}^7 \left[\frac{|\vec{w}_{(1)C,n}| \times |\vec{w}_{(2)n}| \times |\vec{w}_{(O)n}|}{(|\vec{w}_{(1)}| \times |\vec{w}_{(2)n}| \times |\vec{w}_{(O)n}|)} \right], \sum_{n=1}^7 \left[\frac{|\vec{w}_{(1)D,n}| \times |\vec{w}_{(2)n}| \times |\vec{w}_{(O)n}|}{(|\vec{w}_{(1)}| \times |\vec{w}_{(2)n}| \times |\vec{w}_{(O)n}|)} \right] \right\}} \\
& \times 100
\end{aligned} \tag{24}$$

I_i = relative importance of each input variable (%)

i = input variable (A : $i = 1$, B : $i = 2$, C : $i = 3$, D : $i = 4$)

n = number of neuron

$\vec{w}_{(1)i,n}$ = weight of input variable ‘i’ in first hidden layer n^{th} neuron

$\vec{w}_{(2)n}$ = weight of second hidden layer n^{th} neuron

$\vec{w}_{(O)n}$ = weight in output layer n^{th} neuron

Table 24. Comparison of network topologies with various hidden layers and neurons for DCF removal

Topology	MSE	R				Topology	MSE	R			
		Training	Validating	Testing	All			Training	Validating	Testing	All
4:6:2	1.563	0.99998	0.99945	0.99889	0.99972	4:8:6:2	5.010	0.97921	0.99943	0.99833	0.98471
4:7:2	0.883	0.99998	0.99971	0.99958	0.99988	4:8:7:2	44.047	0.99919	0.98558	0.98893	0.99566
4:8:2	35.090	0.97477	0.99149	0.99345	0.97934	4:8:8:2	0.375	0.99996	0.99988	0.99959	0.99989
4:9:2	34.240	0.99690	0.98963	0.99693	0.99569	4:8:9:2	49.838	0.99998	0.98699	0.99957	0.99761
4:10:2	1.780	0.99992	0.99948	0.99915	0.99968	4:8:10:2	1.371	0.99996	0.99959	0.99994	0.99990
4:6:6:2	1.539	0.99997	0.99960	0.99504	0.99919	4:9:6:2	0.651	0.99991	0.99982	0.99819	0.99950
4:6:7:2	3.875	0.99944	0.99886	0.99944	0.99932	4:9:7:2	97.258	0.99993	0.97009	0.96890	0.99091
4:6:8:2	6.506	0.98663	0.99784	0.94417	0.98160	4:9:8:2	3.143	0.99803	0.99956	0.99729	0.99814
4:6:9:2	0.718	0.99991	0.99978	0.99994	0.99989	4:9:9:2	186.735	0.96538	0.97606	0.98129	0.96832
4:6:10:2	3.743	0.99998	0.99912	0.99843	0.99956	4:9:10:2	0.875	0.99983	0.99974	0.99906	0.99969
4:7:6:2	0.119	0.99998	0.99996	0.99938	0.99988	4:10:6:2	0.925	0.99999	0.99976	0.99954	0.99988
4:7:7:2	0.939	0.99990	0.99981	0.99986	0.99986	4:10:7:2	0.389	0.99992	0.99986	0.99998	0.99992
4:7:8:2	1.395	0.99992	0.99965	0.99991	0.99987	4:10:8:2	35.807	0.98145	0.98867	0.98104	0.98217
4:7:9:2	8.218	0.99966	0.99791	0.99731	0.99895	4:10:9:2	65.736	0.99996	0.97923	0.97732	0.99363
4:7:10:2	0.318	0.99992	0.99989	0.99938	0.99978	4:10:10:2	0.328	0.99992	0.99991	0.99997	0.99992

Table 25. Values of weights and biases for each layer and neuron in equation (19)

n	Hidden layer 1 ($\vec{w}_{(1)}$)					Hidden layer 2 ($\vec{w}_{(2)}$)								Output layer($\vec{w}_{(o)}$)						
	$\vec{w}_{(1)A,n}$	$\vec{w}_{(1)B,n}$	$\vec{w}_{(1)C,n}$	$\vec{w}_{(1)D,n}$	$b_{(1)n}$	$\vec{w}_{(2)n}$							$b_{(2)n}$	$\vec{w}_{(o)n}$						$b_{(o)n}$
1	0.63279	-0.29871	1.0963	-1.0941	-3.1067	-0.26584	-1.7312	-0.7483	-0.11563	0.62519	-0.53313	0.52169	-1.5352	1.1144	-0.73327	0.38917	-0.19588	-0.17002	-0.58567	1.2911
2	1.2833	1.9841	-0.63807	2.1241	-1.0701	-0.65548	0.38708	-1.0705	0.12785	-0.77455	-0.8866	1.349	0.81811	-0.07601	0.17659	0.065514	-0.35362	0.59671	0.46051	0.508
3	-0.95818	0.70398	-0.30837	2.6539	0.71392	0.36527	0.2364	0.7995	0.69437	-0.81419	0.32822	0.25989	-0.21014							
4	0.87943	-2.0162	1.1721	0.73209	0.57266	-0.8857	-0.02743	1.2862	1.1771	0.19621	-0.61172	-0.9731	-0.5144							
5	1.7033	1.519	0.58554	1.0936	0.46189	-0.02853	1.1366	-0.85273	0.65838	1.1558	-0.0337	-0.05001	-1.5589							
6	-0.6799	0.93057	2.1696	-0.22559	-1.2426	-0.69579	-0.96196	-1.0541	1.001	0.46281	0.67033	-0.90866	-1.6015							
7	-0.94945	-1.605	0.80626	-1.2467	-1.9396															

Table 26. Observed removal rates, final pH and predicted values from ANN modeling for DCF adsorption (Topology 4:7:6:2)

Ex.	Input variable				DCF removal rate (%)		Final pH	
	Initial pH	MIL-100(Fe) dosage (g/L)	Initial DCF concentration (mg/L)	Temperature (°C)	Observed	Predicted-ANN	Observed	Predicted-ANN
1	5.0	0.8	60	30	87.9±0.05	87.7	4.62±0.02	4.69
2	11.0	0.8	60	30	16.8±0.82	16.6	5.99±0.02	5.93
3	8.0	0.4	60	30	77.7±0.15	77.7	5.02±0.02	5.15
4	8.0	1.2	60	30	89.5±0.20	89.2	4.70±0.06	4.63
5	8.0	0.8	60	10	85.4±1.51	86.8	5.38±0.08	5.46
6	8.0	0.8	60	50	76.5±0.16	76.9	5.12±0.02	5.17
7	8.0	0.8	20	30	75.2±0.44	75.5	4.53±0.03	4.62
8	8.0	0.8	100	30	83.6±0.23	83.5	5.24±0.03	5.19
9	6.5	0.6	40	20	86.4±0.36	86.6	5.08±0.02	5.01
10	6.5	0.6	80	20	87.1±0.17	87.1	5.48±0.06	5.43
11	6.5	0.6	40	40	76.8±0.12	77.9	4.73±0.01	4.86
12	6.5	0.6	80	40	81.6±0.44	81.8	5.03±0.00	5.03
13	6.5	1.0	40	20	90.0±0.55	90.1	4.74±0.03	4.69
14	6.5	1.0	80	20	90.8±0.63	89.7	5.17±0.00	5.20
15	6.5	1.0	40	40	80.1±0.08	80.1	4.53±0.00	4.58
16	6.5	1.0	80	40	84.8±0.21	85.4	4.84±0.03	4.79
17	9.5	0.6	40	20	70.8±0.89	70.8	5.32±0.02	5.34
18	9.5	0.6	80	20	75.8±0.31	75.7	5.53±0.02	5.46
19	9.5	0.6	40	40	71.7±0.48	71.5	5.09±0.00	4.95
20	9.5	0.6	80	40	79.8±0.05	79.6	5.22±0.01	5.10
21	9.5	1.0	40	20	78.1±2.14	78.5	5.14±0.01	5.16
22	9.5	1.0	80	20	85.7±0.62	85.6	5.41±0.04	5.53
23	9.5	1.0	40	40	76.0±0.24	76.2	5.05±0.04	4.90
24	9.5	1.0	80	40	83.7±0.22	83.6	5.14±0.06	5.24
25	8.0	0.8	60	30	86.3±0.11	86.4	4.93±0.01	4.95
26	8.0	0.8	60	30	86.3±0.46	86.4	4.91±0.02	4.95
27	8.0	0.8	60	30	86.6±0.58	86.4	4.92±0.01	4.95
28	8.0	0.8	60	30	86.4±0.19	86.4	4.90±0.01	4.95

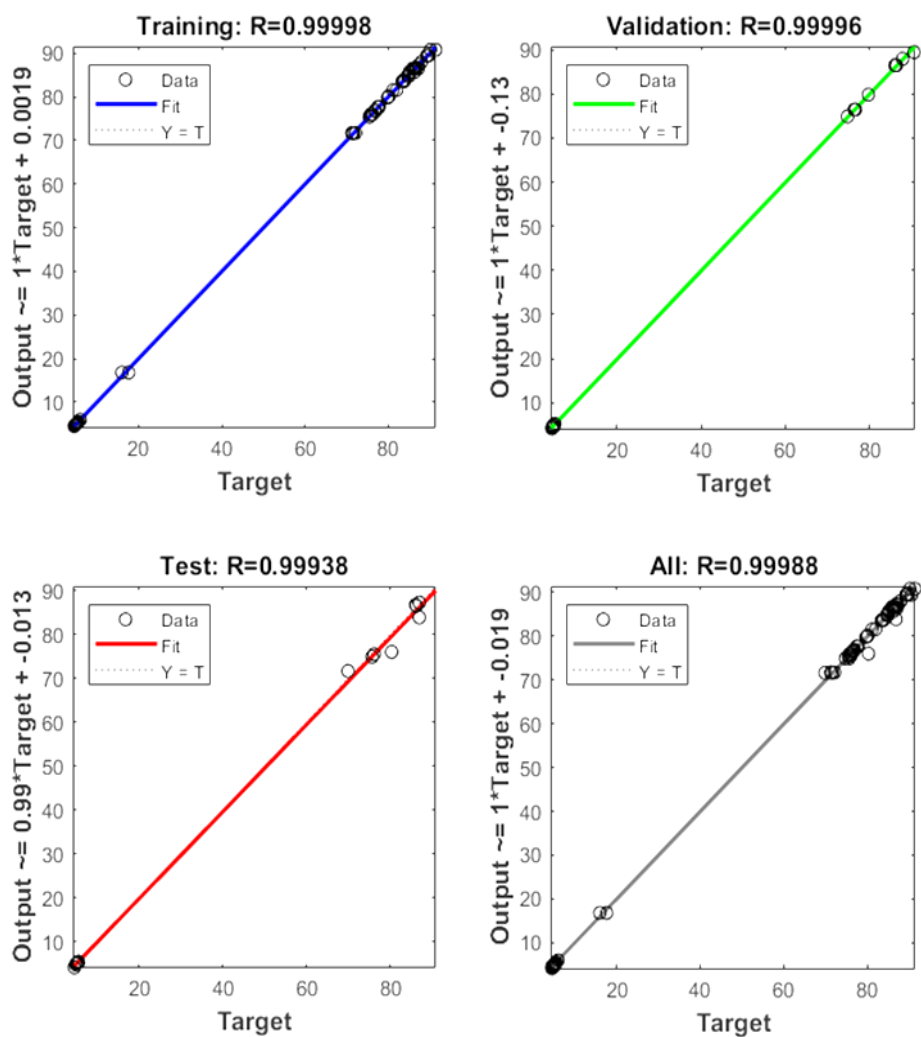


Fig. 28. Linear fit for experimental and predicted DCF removal rate and final pH

Table 27. Additional experimental conditions along with observed and predicted from the ANN model values for DCF removal rates and final pH

Ex.	Input variable				DCF removal rate (%)		Final pH	
	Initial pH (A)	Adsorbent dose (B)	Initial DCF conc. (C)	Temperature (D)	Observed	Predicted	Observed	Predicted
A1	8.2	0.7	62.0	42	80.3	77.8	4.86	4.91
A2	5.3	0.8	51.1	28	85.7	82.6	4.74	4.69
A3	6.0	0.7	82.4	37	87.1	83.7	4.88	5.08
A4	8.2	0.7	62.0	42	80.1	77.8	4.82	4.91
A5	5.3	0.8	51.1	28	87.3	82.6	4.71	4.69
A6	6.0	0.7	82.4	37	87.2	83.7	4.87	5.08

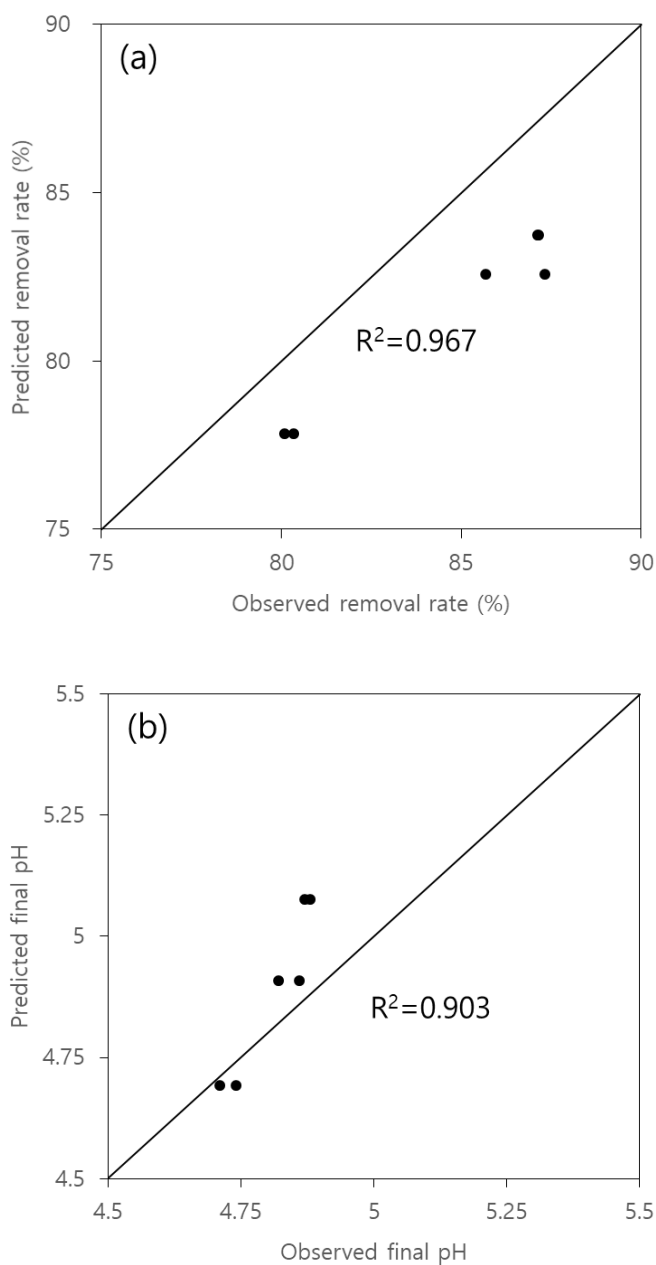


Fig. 29. Diagnostic plots between observed and predicted values from additional experiments: (a) DCF removal rate; and (b) final pH

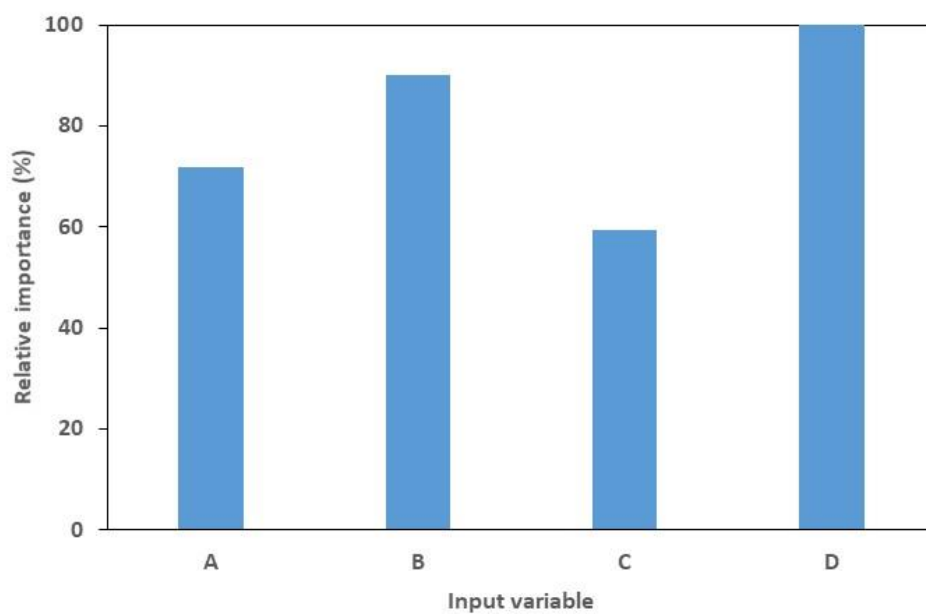


Fig. 30. Relative importance of four input variables on the DCF removal rate

Table 28. Optimum condition for DCF removal by the MIL-100(Fe) from ANN model

Input variable				DCF removal rate (%)
Initial pH (A)	Adsorbent dose (B)	Initial DCF conc. (C)	Temperature (D)	
6.1	0.5	63	22	99.9
6.7	1.1	67	26	99.8
8.0	1.1	47	22	99.7
7.3	0.9	52	28	99.6
6.6	0.9	64	31	99.5

5. Conclusions

The most conventional MIL-100(Fe) synthesis is performed by hydrothermal synthesis method at high temperatures above 160 °C. However, MIL-100(Fe) synthesized at room temperature has a simpler process, does not require an apparatus such as Teflon-lined steel autoclave, and has a yield of about 2 – 3 times higher than hydrothermal synthesized MIL-100(Fe). Characterization was performed to determine the physicochemical properties of the synthesized MIL-100(Fe), and applied as adsorbent to remove Rhodamine B (RhB) and Diclofenac (DCF) from aqueous solutions.

Batch experiments were conducted for RhB and DCF under single-parameter experiment and multi-parameter experiment conditions, and the adsorption mechanism was identified through pH experiments. In the case of RhB removal, π - π interaction and electrostatic attraction acted at pH 4 - 10, and in the case of DCF removal, π - π interaction and hydrogen bonding acted. The maximum adsorption capacity for RhB is 61.845 mg g⁻¹ and DCF is 414.581 mg g⁻¹.

Further, multi-parameter models were employed to model and

optimized the RhB and DCF removal by the MIL-100(Fe). The RSM model with cubic regression equation was developed for RhB removal. The regressor variable of pH had a larger coefficient value indicating that pH had a higher impact on the RhB removal rate than other input variables. The ANN model with the topology of 3:8:1 and 4:7:6:2 were developed to adequately model for RhB and DCF removal, respectively. The optimum conditions for RhB and DCF removal rate were predicted using the developed ANN model. The optimum RhB removal rate (>99.9%) was found at pH 5.3, adsorbent dose 2.0 g L^{-1} , and initial RhB concentration 73 mg L^{-1} through the prediction of the modeled ANN. The optimum DCF removal rate (99.9%) was found at initial pH 6.1, adsorbent dose 0.5 g L^{-1} , initial DCF concentration 63 mg L^{-1} , and temperature 22°C through the prediction of the modeled ANN. In addition, pH and temperature were the most important input variable affecting the RhB and DCF removal rate, respectively.

This study demonstrated that the MIL-100(Fe) synthesized at room temperature, which has high surface area and great water stability, effective in removing RhB and DCF under experimental conditions as an adsorbent with high adsorption capacity. However, since MOF is required

a separated treatment process due to their powder form, there is a limit to practical application in the field. Therefore, adsorbent reforming to increase the practicality of MOF or adsorption experiments and modeling for actual industrial wastewater are required.

6. References

- Abbasi AR, Karimi M, Daasbjerg K. 2017. Efficient removal of crystal violet and methylene blue from wastewater by ultrasound nanoparticles Cu-MOF in comparison with mechanosynthesis method. *Ult. Sonochem.* 37: 182-191.
- Adeyemo AA, Adeoye IO, Bello OS. 2012. Metal organic frameworks as adsorbents for dye adsorption: overview, prospects and future challenges. *Toxic. Environ. Chem.* 94: 1846-1863.
- Antunes M, Esteves VI, Guegan R, Crespo JS, Fernandes AN, Giovanela M. 2012. Removal of diclofenac sodium from aqueous solution by Isabel grape bagasse. *Chem. Eng.* 192: 114-121.
- Aslam S, Zeng J, Subhan F, Li M, Lyu F, Li Y, Yan Z. 2017. In situ one-step synthesis of $\text{Fe}_3\text{O}_4@\text{MIL-100}(\text{Fe})$ core-shells for adsorption of methylene blue from water. *J. Colloid, Int. Sci.* 505: 186-195.
- Ayati A, Shahrak MN, Tanhaei B, Sillanpaa M. 2016. Emerging adsorptive removal of azo dye by metal-organic frameworks. *Chemosphere* 160: 30-44.

- Bagheri H, Daliri R, Roostaie A. 2013. A novel magnetic poly(aniline-naphthylamine)-based nanocomposite for micro solid phase extraction of rhodamine B. *Analy. Chimica Acta* 794: 38-46.
- Baziar M, Azari A, Karimaei M, Gupta VK, Agarwal S, Sharafi K, Maroosi M, Shariatifar N, Dobaradaran S. 2017. MWCNT-Fe₃O₄ as a superior adsorbent for microcystins LR removal: investigation on the magnetic adsorption separation, artificial neural network modeling, and genetic algorithm optimization. *J. Mol. Liq.* 241: 102-113.
- Benotti MJ, Trenholm RA, Vanderford BJ, Holady JC, Stanford BD, Snyder SA. 2009. Pharmaceuticals and endocrine disrupting compounds in U.S. drinking water. *Environ. Sci. Technol.* 43(3): 597-603.
- Bhadra BN, Ahmed I, Kim SH, Jung SH. 2017. Adsorptive removal of ibuprofen and diclofenac from water using metal-organic framework-derived porous carbon. *Chem. Eng. J.* 314: 50-58.
- Binaeian E, Motaghedi N, Maleki S & Arjmandi M. 2020. Ibuprofen uptake through dimethyl ethylenediamine modified MOF: optimization of the adsorption process by response surface methodology technique. *J. Dis. Sci. Technol.* 1810696.

- Cai J, Wang X, Zhou Y, Jiang L, Wang C. 2016. Selective adsorption of arsenate and the reversible structure transformation of the mesoporous metal-organic framework MIL-100(Fe). *Phys. Chem. Chem. Phys.* 18: 10864-10867.
- Cui W, Kang X, Zhang X, Cui X. 2019. Gel-like ZnO/Zr-MOF(bpy) nanocomposite for highly efficient adsorption of rhodamine B dye from aqueous solution. *J. Phys, Chem. Solid.* 134: 165-175.
- De Luna MDG, Murniati, Budianta W, Rivera KKP, Arazo RO. 2017. Removal of sodium diclofenac from aqueous solution by adsorbents derived from cocoa pod husks. *J. Environ. Chem. Eng.* 5: 1465-1474.
- Duan S, Li J, Liu X, Wang Y, Zeng S, Shao D, Hayat T. 2016. HF-free synthesis of nanoscale metal-organic framework NMIL-100(Fe) as an efficient dye adsorbent. *ACS Sustainable Chem. Eng.* 4: 3368-3378.
- Esfandiari K, Ghoreyshi AA, Jahanshahi M. 2017. Using artificial neural network and ideal adsorbed solution theory for predicting the CO₂/CH₄ selectivities of metal-organic frameworks: a comparative study. *Ind. Eng. Chem. Res.* 56: 14610-14622.
- Esfafil L, Gharib M, Morsali A. 2019. The targeted design of dual-

- functional metal-organic frameworks (DF-MOFs) as highly efficient adsorbents for Hg^{2+} ions: synthesis for purpose. Dalton Trans. 48: 17831-17839.
- Esrafil L, Gharib M, Morsali A. 2019. Selective detection and removal of mercury ions by dual-functionalized metal-organic frameworks: design-for-purpose. New J. Chem. 43: 18079-18091.
- Fan J, Chen D, Li N, Xu Q, Li H, He J, Lu J. 2018. Adsorption and biodegradation of dye in wastewater with $\text{Fe}_3\text{O}_4@\text{MIL-100}(\text{Fe})$ core-shell bio-nanocomposites. Chemosphere 191: 315-323.
- Fang Y, Wen J, Zeng G, Jia F, Zhang S, Peng Z, Zhang H. 2018. Effect of mineralizing agents on the adsorption performance of metal-organic framework MIL-100(Fe) towards chromium. Chem. Eng. J. 337: 532-540.
- Feng M, Zhang P, Zhou HC, Sharma VK. 2018. Water-stable metal-organic frameworks for aqueous removal of heavy metals and radionuclides: a review. Chemosphere 209: 783-800.
- Furukawa H, Cordova KE, O'Keeffe M, Yaghi OM. 2013. The chemistry and applications of metal-organic frameworks. Science 341: 1230444.
- Gaddekar MR, Ahammed MM. 2019. Modelling dye removal by adsorption

onto water treatment residuals using combined response surface methodology-artificial neural network approach. J. Environ. Manage. 231: 241-248.

Georgiou Y, Perman JA, Bourlinos AB, Deligiannakis Y. 2018. Highly efficient arsenite (As) adsorption by an MIL-100(Fe) Metal-organic framework: Structural and mechanistic insights. J. Phys. Chem. 122: 4859-4869.

Ghaedi AM, Vafaei A. 2017. Applications of artificial neural networks for adsorption removal of dyes from aqueous solution: a review. Adv. Colloid, Int. Sci. 245: 20-39.

Ghaedi M, Daneshfar A, Ahmadi A, Momeni MS. 2015. Artificial neural network-genetic algorithm based optimization for the adsorption of phenol red (PR) onto gold and titanium dioxide nanoparticles loaded on activated carbon. J. Ind. Eng. Chem. 21: 587-598.

Ghemit R, Makhoulfi A, Djebri N, Flilissa A, Zerroual L, Boutahala M. 2019. Adsorptive removal of diclofenac and ibuprofen from aqueous solution by organobentonites: Study in single and binary systems. Groundw. Sustain Dev. 8: 520-529.

- Guesh K, Caiuby CAD, Mayoral A, Diaz-Garcia M, Diaz I, Sanchez-Sanchez M. 2017. Sustainable preparation of MIL-100(Fe) and its photocatalytic behavior in the degradation of methyl orange in water. *Cryst. Growth Des.* 17: 1806-1813.
- Haque E, Jun JW, Jung SH. 2011. Adsorptive removal of methyl orange and methylene blue from aqueous solution with a metal-organic framework material, iron terephthalate (MOF-235). *J. Hazard. Mater.* 185: 507-511.
- Hasan Z, Khan NA, Jung SH. 2016. Adsorptive removal of diclofenac sodium from water with Zr-based metal-organic frameworks. *Chem. Eng. J.* 284: 1406-1413.
- He S, Wang J, Ye L, Zhang Y, Yu J. 2014. Removal of diclofenac from surface water by electron beam irradiation combined with a biological aerated filter. *Radiat. Phys. Chem.* 105: 104-108.
- Huo SH, Yan XP. 2012. Metal-organic framework MIL-100(Fe) for the adsorption of malachite green from aqueous solution. *J. Mater. Chem.* 22: 7449.
- Jahed-Armaghani D, Shoib RSNSBR, Faizi K, Rashid ASA. 2017. Developing a hybrid PSO-ANN model for estimating the ultimate bearing

- capacity of rock-socketed piles. *Neural Comput, Applic.* 28: 391-405.
- Jarrah A, Farhadi S. 2020. Encapsulation of $K_6P_2W_{18}O_{62}$ into magnetic nanoporous $Fe_3O_4/MIL-101(Fe)$ for highly enhanced removal of organic dyes. *J. Solid Sta. Chem.* 285: 121264.
- Jin L, Zhao X, Qian X, Dong M. 2018. Nickel nanoparticles encapsulated in porous carbon and carbon nanotube hybrids from bimetallic metal-organic-frameworks for highly efficient adsorption of dyes. *J. Colloid, Int. Sci.* 509: 245-253.
- Joseph L, Jun BM, Jang M, Park CM, Munoz-Senmache JC, Hernandez-Maldonado AJ, Heyden A, Yu M, Yoon YM. 2019. Removal of contaminants of emerging concern by metal-organic framework nanoadsorbents: A review. *Chem. Eng. J.* 369: 928-946.
- Karami A, Sabouni R, Ghommam M. 2020. Experimental investigation of competitive co-adsorption of naproxen and diclofenac from water by an aluminum-based metal-organic framework. *J. Mol. Liq.* 305: 112808.
- Kokcam-Demir U, Goldman A, Esrafil L, Gharib M, Morsali A, Weingart O, Janiak C. 2020. Coordinatively unsaturated metal sites (open metal sites) in metal-organic frameworks: design and applications. *Chem. Soc. Rev.*

49: 2751-2798.

Lee JG, Joshi BN, Samuel E, An SP, Swihart MT, Lee JS, Hwang YK, Chang JS, Yoon SS. 2017. Supersonically sprayed gas- and water-sensing MIL-100(Fe) films. *J. Alloy. Compd.* 722: 996-1001.

Li S, Cui J, Wu X, Zhang X, Hu Q, Hou X. 2019. Rapid in situ microwave synthesis of Fe₃O₄@MIL-100(Fe) for aqueous diclofenac sodium removal through integrated adsorption and photodegradation. *J. Hazard Mater.* 373: 408-416.

Li Y, Yan X, Hu X, Feng R, Zhou M. 2019. Trace pyrolyzed ZIF-67 loaded activated carbon pellets for enhanced adsorption and catalytic degradation of rhodamine B in water. *Chem Eng. J.* 375: 122003.

Liu H, Ren X, Chen L. 2016. Synthesis and characterization of magnetic metal-organic framework for the adsorptive removal of rhodamine B from aqueous solution. *J. Ind. Eng. Chem.* 34: 278-285.

Liu W, Shen X, Han Y, Liu Z, Dai W, Dutta A, Kumar A, Liu J. 2019. Selective adsorption and removal of drug contaminants by using an extremely stable Cu(II)-based 3D metal-organic framework. *Chemosphere* 215: 524-531.

- Liu Y, Zhao Y, Wang J. 2020. Fenton/fenton-like processes with in-situ production of hydrogen peroxide/hydroxyl radical for degradation of emerging contaminants: Advances and prospects. *J. Hazard Mater.* 404: 124191.
- Luo Z, Fan S, Liu J, Liu W, Shen X, Wu C, Huang Y, Huang G, Huang H, Zheng M. 2018. A 3D stable metal-organic framework for highly efficient adsorption and removal of drug contaminants from water. *Polymers* 10: 209.
- Ma S, Tong L, Ye F, Xiao J, Benard P, Chahine R. 2019. Hydrogen purification layered bed optimization based on artificial neural network prediction of breakthrough curves. *Int. J. Hydrogen Energy* 44: 5324-5333.
- Mahmoodi NM, Oveisi M, Taghizadeh A, Taghizadeh M. 2019. Novel magnetic amine functionalized carbon nanotube/metal-organic framework nanocomposites: from green ultrasound-assisted synthesis to detailed selective pollutant removal modelling from binary systems. *J. Hazard. Mater.* 368: 746-759.
- Miao H, Hou H, Zhang W, Yang G. 2020. A ligand-doped silver triazolate MOF on the removal of diclofenac sodium via anion exchange.

- ChemistrySelect 5: 11948-11954.
- Mohammadifard Z, Saboori R, Mirbagheri NS, Sabbaghi S. 2019. Heterogeneous photo-fenton degradation of formaldehyde using MIL-100(Fe) under visible light irradiation. Environ. Pollut. 251: 783-791.
- Moreno-Villoslada I, Jofre M, Miranda V, Gonzalez R, Sotelo T, Hess S, Rivas BL. 2006. pH dependence of the interaction between Rhodamine B and the water-soluble poly(sodium 4-styrenesulfonate). J. Phys. Chem. B 110: 11809-11812.
- Nair AT, Makwana AR, Ahammed MM. 2014. The use of response surface methodology for modelling and analysis of water and wastewater treatment processes: a review. Water Sci. Technol. 69: 464-478.
- Nasrollahpour A, Moradi SE. 2017. Hexavalent chromium removal from water by ionic liquid modified metal-organic frameworks adsorbent. Micro, Meso. Mater. 243: 47-55.
- Navarathna CM, Dewage NB, Karunanayake AG, Farmer EL, Perez F, Hassan EB, Mlsna TE, Pittman Jr. CU. 2020. Rhodamine B adsorptive removal and photocatalytic degradation on MIL-53-Fe-MOF/magnetic magnetite/biochar composites. J. Inorg. Organomet. Polym. 30: 214-229.

- Nehra M, Dilbaghi N, Singhal NK, Hassan AA, Kim KH, Kumar S. 2019. Metal organic frameworks MIL-100(Fe) as an efficient adsorptive material for phosphate management. *Environ. Res.* 169: 229-236.
- Oh JY. 2009. Study for analysis and fate of pharmaceuticals in wastewater treatment plants. Busan University.
- Samui P, Kim D, Ghosh C. 2018. Integrating disaster science and management: global case studies in mitigation and recover. Elsevier Science Publishing Co Inc., Cambridge, MA, USA, pp 47-49.
- Seo PW, Bhadra BN, Ahmed I, Khan NA, Jung SH. 2016. Adsorptive removal of pharmaceuticals and personal care products from water with functionalized metal-organic frameworks: remarkable adsorbents with hydrogen-bonding abilities. *Sci. Rep.* 6: 34462.
- Sharafi K, Pirsaeheb M, Gupta VK, Agarwal S, Moradi M, Vasseghian Y, Dragoi EN. 2019. Phenol adsorption on scoria stone as adsorbent – application of response surface method and artificial neural networks. *J. Mol. Liq.* 274: 699-714.
- Sharma J, Sukriti, Anand P, Pruthi V, Chaddha AS, Bhatia J, Kaith BS. 2017. RSM-CCD optimized adsorbent for the sequestration of carcinogenic

- rhodamine-B: Kinetic and equilibrium studies. *Mater. Chem. Phys.* 196: 270-283.
- Tan F, Liu M, Li K, Wang Y, Wang J, Guo X, Zhang G, Song C. 2015. Facile synthesis of size-controlled MIL-100(Fe) with excellent adsorption capacity for methylene blue. *Chem. Eng. J.* 281: 360-367.
- Tehrani AA, Esrafil L, Abedi S, Morsali A, Carlucci L, Proserpio DM, Wang J, Junk PC, Liu T. 2017. Urea metal-organic frameworks for nitro-substituted compounds sensing. *Inorg. Chem.* 56: 1446-1454.
- Tran TV, Nguyen DTC, Nguyen TT, Nguyen CV, Vo DVN, Nguyen TD. 2020. High performance of $\text{Mn}_2(\text{BDC})_2(\text{DMF})_2$ -derived MnO@C nanocomposite as superior remediator for a series of emergent antibiotics. *J. Mol. Liq.* 308: 113038.
- Vo TK, Bae YS, Chang BJ, Moon SY, Kim JH, Kim JS. 2019. Highly CO selective Cu-doped MIL-100(Fe) adsorbent with high CO/ CO_2 selectivity due to π complexation: Effects of Cu loading and activation temperature. *Micro, Meso. Mater.* 274: 17-24.
- Wang J, Chu L. 2016. Irradiation treatment of pharmaceutical and personal care products (PPCPs) in water and wastewater: An overview. *Radiat.*

- Phys. Chem. 125: 56-64.
- Wang J, Guo X. 2020. Adsorption isotherm models: Classification, physical meaning, application and solving method. *Chemosphere* 258: 127279.
- Wang J, Guo X. 2020. Adsorption kinetic models: Physical meanings, applications, and solving methods. *J. Hazard Mater.* 390: 122156.
- Wang J, Wang S. 2019. Preparation, modification and environmental application of biochar: A review. *J. Clean Prod.* 227: 1002-1022.
- Wang J, Zhuan R, Chu L. 2019. The occurrence, distribution and degradation of antibiotics by ionizing radiation: An overview. *Sci. Total Environ.* 646: 1385-1397.
- Wang J, Chen H. 2020. Catalytic ozonation for water and wastewater treatment: Recent advances and perspective. *Sci. Total Environ.* 704: 135249.
- Wang J, Chu L, Wojnarovits L, Takacs E. 2020. Occurrence and fate of antibiotics, antibiotic resistant genes (ARGs) and antibiotic resistant bacteria (ARB) in municipal wastewater treatment plant: An overview. *Sci. Total Environ.* 744: 140997.
- Wang R, Guo W, Li X, Liu Z, Liu H, Ding S. 2017. Highly efficient MOF-based self-propelled micromotors for water purification. *RSC Adv.* 7:

42462-42467.

Wang Y, Liu J, Kang D, Wu C, Wu Y. 2017. Removal of pharmaceuticals and personal care products from wastewater using algae-based technologies: a review. *Rev. Environ. Sci. Biotechnol.* 16: 717-735.

Wei F, Chen D, Liang Z, Zhao S. 2018. Comparison study on the adsorption capacity of rhodamine B, congo red, and orange on Fe-MOFs. *Nanomaterials* 8: 248.

Wu L, Du C, He J, Yang Z, Li H. 2020. Effective adsorption of diclofenac sodium from neutral aqueous solution by low-cost lignite activated cokes. *J. Hazard Mater.* 384: 121284.

Yang C, Wu S, Cheng J, Chen Y. 2016. Indium-based metal-organic framework/graphite oxide composite as an efficient adsorbent in the adsorption of rhodamine B from aqueous solution. *J. Alloys, Comp.* 687: 804-812.

Yilmaz E, Sert E, Atalay FS. 2016. Synthesis, characterization of a metal organic framework: MIL-53(Fe) and adsorption mechanisms of methyl red onto MIL-53(Fe). *J. Taiwan Ins. Chem. Eng.* 65: 323-330.

Zhan XQ, Tsai FC, Xie L, Zhang KD, Liu HL, Ma N, Shi D, Jiang T. 2018. Ligands-coordinated Zr-based MOF for wastewater treatment.

Nanomaterials 8: 655.

Zhang J, Li F, Sun Q. 2018. Rapid and selective adsorption of cationic dyes by a unique metal-organic framework with decorated pore surface. *Appl. Surf. Sci.* 440: 1219-1226.

Zhang H, Wen J, Fang Y, Zhang S, Zeng G. 2019. Influence of fulvic acid on Pb() removal from water using a post-synthetically modified MIL-100(Fe). *J. Colloid, Inter. Sci.* 551: 155-163.

Zhang W, Li N, Xiao T, Tang W, Xiu G. 2019. Removal of antimonite and antimonite from water using Fe-based metal-organic frameworks: the relationship between framework structure and adsorption performance. *J. Environ. Sci.* 86: 213-224.

Zhao X, Liu S, Tang Z, Niu H, Cai Y, Meng W, Wu F, Giesy JP. 2015. Synthesis of magnetic metal-organic framework (MOF) for efficient removal of organic dyes from water. *Sci. Rep.* 5: 11849.

Zheng X, Wang J, Xue X, Liu W, Kong Y, Cheng R, Yuan D. 2018. Facile synthesis of Fe₃O₄@MOF-100(Fe) magnetic microspheres for the adsorption of diclofenac sodium in aqueous solution. *Environ. Sci. Pollut. Res.* 25: 31705-31717.

- Zhou HC, kitagawa S. 2014. Metal-organic frameworks (MOFs). Chem. Soc. Rev. 43: 5415-5418.
- Zhu TT, Zhang ZM, Chen WL, Liu ZJ, Wang EB. 2016. Encapsulation of tungstophosphoric acid into harmless MIL-101(Fe) for effectively removing cationic dye from aqueous solution. RSC Adv. 6: 81622-81630.
- Zhu Y, Zhao C, Liang J, Shang R, Zhu X, Ding L, Deng H, Zheng H, Strathmann TJ. 2019. Rapid removal of diclofenac in aqueous solution by soluble Mn(III)_(aq) generated in a novel electro-activated carbon fiber-permanganate (E-ACF-PM) process. Water Res. 165: 114975.
- Zhuan R, Wang J. 2020. Degradation of diclofenac in aqueous solution by ionizing radiation in the presence of humic acid. Sep. Purif. Technol. 234: 116079.
- Zhuang S, Cheng R, Wang J. 2019. Adsorption of diclofenac from aqueous solution using UiO-66-type metal-organic frameworks. Chem. Eng. J. 359: 354-362.
- Zhuang S, Liu Y, Wang J. 2019. Mechanistic insight into the adsorption of diclofenac by MIL-100: Experiments and theoretical calculations. Environ. Pollut. 253: 616-624.

국문 초록

본 연구의 목적은 금속-유기 복합체 (Metal organic framework, MOF)를 사용하여 수용액에서 오염 물질을 제거하는 것이다. MOF는 금속 클러스터와 유기 링커 사이의 강력한 배위 결합으로 만들어진 다공성 결정형 복합체로, 표면적이 크고 구조적 유연성이 있다는 특성을 가지고 있다. MOF 중에서도 상온에서 합성한 MIL-100(Fe)는 철 (Fe)과 Trimesic acid 를 사용하였고, 환경 친화적이며, 수중 안정성이 높고, 높은 흡착효율을 보이는 흡착제이다.

본 연구에서는 MIL-100(Fe)를 흡착제로 사용하여 수중의 Rhodamine B (RhB)와 Diclofenac (DCF)를 제거하였다. 단일 매개 변수 및 다중 매개 변수 실험 조건에서 RhB와 DCF 각각에 대해 흡착 회분 실험을 진행하였다. MIL-100(Fe)을 이용한 RhB의 최대 흡착능은 61.845 mg g^{-1} 이고, DCF의 최대흡착능은 $414.581 \text{ mg g}^{-1}$ 이다. pH 실험 결과, RhB 흡착의 주된 메커니즘은 π - π 결합과 정전기적 인력이며, DCF 흡착의 주된 메커니즘은 π - π 결합과 수소 결합이다.

또한, 반응표면방법론 (RSM)과 인공신경망 (ANN)을 사용하여 중심합성설계 (CCD) 매트릭스 조건 범위에서 RhB와 DCF 제거에 대한 다중 매개 변수 실험을 모델링하고 최적화하였다. RSM 모델링에서는 RhB 제거를 위해 3차 회귀 모델이 사용되었으며, 변수

중에서 가장 큰 회귀 변수 값을 갖는 pH가 RhB 제거율에 가장 큰 영향을 미친다는 것을 나타낸다. ANN 모델링을 통한 최적의 RhB 제거율을 보이는 조건은 3:8:1 의 ANN 구조에서 pH 5.3, 흡착제 용량 2.0 g L^{-1} , 초기 RhB 농도 73 mg L^{-1} 이다. 최적의 DCF 제거율을 보이는 조건은 4:7:6:2 의 ANN 구조에서 초기 pH 6.1, 흡착제 용량 0.5 g L^{-1} , 초기 DCF 농도 63 mg L^{-1} , 반응온도 $22 \text{ }^{\circ}\text{C}$ 이다.

본 연구 결과를 통해 상온에서 합성한 MIL-100(Fe)이 수중 RhB와 DCF를 제거에 높은 흡착능을 보이는 효과적인 흡착제임을 확인하였고, RSM과 ANN 모델이 다중 매개 변수 모델로서 RhB와 DCF 제거를 최적화하고 예측하는 데 효과적인 모델임을 확인하였다.

주요어 : 금속-유기 복합체, MIL-100(Fe), 흡착, Rhodamine B, Diclofenac, 반응표면방법론, 인공신경망

학 번 : 2019-22277